

Study of Photovoltaic Cells Fabricated with Monocrystalline Bridgman-grown CuInSe_2

Hui Du
(B.Eng, Harbin Institute of Technology, China)

**A thesis submitted to the Faculty of Graduate Studies and Research in
partial fulfillment of the requirements for the degree of Master of
Engineering**

**Department of Electrical Engineering,
McGill University,
Montreal, Quebec,
Canada.**

PSE

June 2003

2023252

ABSTRACT

Using a vertical Bridgman method, ingots of the chalcopyrite semiconductor CuInSe_2 were prepared containing monocrystals of the compound with dimensions of several millimetres. The ingots were grown from both stoichiometric and nonstoichiometric proportions of the starting elements copper, indium and selenium. Material prepared with excess selenium ($\text{CuInSe}_{2.2}$) showed increased p-type conductivity in the last zone to freeze of the ingot, while material grown with a deficiency ($\text{CuInSe}_{1.8}$) of this element showed n-type behaviour, with extra binary phases, such as InSe , in the last zone to freeze. Ingots with excess copper (Cu_xInSe_2), where x was 1.1, 1.2 and 1.3, showed precipitated copper phase regions in the last zone to freeze and thin copper phase filaments emerging from the ingot end face. The electrical resistivity immediately adjacent to the copper precipitate regions was found to be higher than elsewhere.

Photovoltaic cells were fabricated from wafers cut from the p-type Bridgman-grown ingots with a layer structure $\text{Au-CuInSe}_2\text{-CdS-ZnO-In}$. The gold was evaporated on the back of the wafer, the CdS was deposited by a chemical bath method, the ZnO by rf sputtering and the indium contact stripes on the ZnO were deposited by evaporation. Measurements of dark and illuminated current-voltage characteristics, photoresponse and capacitance-voltage characteristics were made on the fabricated cells. One of these devices indicated a conversion efficiency, without an antireflection coating, of 12.5 % under sunlight on a cell area of 12.6 mm^2 , which is better than on any previous monocrystalline cell. Among the cells, it was found that better photovoltaic performance correlated with a higher hole concentration, as estimated from Mott-Schottky plots.

RÉSUMÉ

En utilisant une méthode de Bridgman verticale, des lingots du semi-conducteur chalcopyrite CuInSe_2 ont été préparés contenant des monocristaux du composé ayant des dimensions de quelques millimètres. Les lingots ont été poussés avec des proportions stoechiométriques et non-stoechiométriques de cuivre, d'indium et de sélénium, les éléments initiaux. Le matériau préparé avec du sélénium en excès ($\text{CuInSe}_{2.2}$) a présenté une conductivité électrique de type p élevée dans la dernière zone de solidification, mais le matériau poussé avec un déficit de cet élément ($\text{CuInSe}_{1.8}$) a présenté une conductivité de type n et des phases binaires supplémentaires, par exemple le InSe , dans la dernière zone de solidification. Les lingots ayant un excès de cuivre (Cu_xInSe_2) où x avait une valeur de 1.1, 1.2 et 1.3, présentaient une phase de cuivre dans la dernière zone de solidification et des filaments minces de phase de cuivre émergeant du bout du lingot. Il a été constaté que la résistivité dans la région adjacente au précipité de cuivre était plus élevée qu'ailleurs.

Des cellules photovoltaïques ont été fabriquées à partir de tranches coupées des lingots de Bridgman de type p à structure en minces couches superposées comme suit : $\text{Au-CuInSe}_2\text{-CdS-ZnO-In}$. L'Or a été évaporé sur l'arrière de la plaque, le CdS a été déposé dans un bain chimique, le ZnO l'a été par pulvérisation cathodique de haute fréquence et les rayures de contact d'indium ont été déposées sur le ZnO par évaporation. Des mesures de caractéristiques courant-tension dans l'obscurité et en milieu illuminé, de photoréponse et de capacité-tension ont été effectuées sur les cellules. Une de ces cellules a indiqué un rendement de conversion, sans une couche antiréfléchissante, de 12.5% pour une aire de 12.6 mm^2 exposée à la lumière du soleil. Ce résultat est supérieur à celui obtenu pour tout dispositif monocristallin antérieur. Parmi les cellules, il a été découvert qu'il existe une

corrélation entre la performance photovoltaïque supérieure et la concentration élevée de trous dans le CuInSe_2 , comme estimé par les traces de Mott-Schottky.

ACKNOWLEDGMENTS

The author would like to express his sincere gratitude to his supervisors, Dr. I. Shih and Dr. C.H. Champness for their patience, guidance and assistance throughout the study.

The author wishes also to thank everyone who gave help or suggestions during this work.

Finally, the author would like to express his gratitude to his wife and parents for their love, encouragement and support during this study.

TABLE OF CONTENTS

ABSTRACT	i
RÉSUMÉ	ii
ACKNOWLEDGEMENTS	iv
TABLE OF CONTENTS	v

1	INTRODUCTION	1
2	SOME PHOTOVOLTAIC FUNDAMENTALS	6
2.1	INTRODUCTION	6
2.2	MAXIMUM PHOTOCURRENT	6
	2.2(a) Wavelength Limitations	7
	2.2(b) Special Simplified Case	8
	2.2(c) Numerical Integration for CuInSe ₂	8
2.3	SIMPLE EQUIVALENT CIRCUIT OF CELL	9
	2.3(a) Current-voltage Relation	9
	2.3(b) I-V Gradients	10
3	BRIDGMAN GROWTH OF CuInSe₂	19
3.1	INTRODUCTION	19
3.2	AMPOULE PREPARATION	20
	3.2(a) Ampoule Formation	20
	3.2(b) Ampoule Cleaning	21
	3.2(c) Boron Nitride Coating	21
3.3	COMPOUND SYNTHESIS	21
	3.3(a) Pellet Etching	22
	3.3(b) Ampoule Pumping and Sealing	22
	3.3(c) Pre-reaction of the Charge	23
3.4	BRIDGMAN GROWTH	23
	3.4(a) Temperature Soak	23
	3.4(b) Ampoule Lowering	24
	3.4(c) Temperature Profile of Bridgman Furnace	25
	3.4(d) Specific Growth Run Conditions	25
3.5	RESULTS	26
	3.5(a) Crystallinity of Ingots	26
	3.5(b) Electrical Evaluation of Ingots	26
	(i) Ingots with selenium nonstoichiometry	27
	(ii) Ingots with copper excess	28

3.6	DISCUSSION	29
4	FABRICATION OF PHOTOVOLTAIC CELLS	46
4.1	INTRODUCTION	46
4.2	CuInSe ₂ WAFER PREPARATION	47
4.2(a)	Wafer Polishing	47
4.2(b)	Wafer Etching	47
4.2(c)	Wafer Annealing	48
4.3	LAYER DEPOSITIONS	48
4.3(a)	CdS Deposition	48
4.3(b)	Gold Back Contact	49
4.3(c)	ZnO Deposition	49
4.4	FURTHER STEPS	50
4.4(a)	ZnO Thickness and Resistivity	50
4.4(b)	Contact Stripes and Cell Mounting	51
5	CELL CHARACTERISTICS UNDER ILLUMINATION	57
5.1	INTRODUCTION	57
5.2	CURRENT-VOLTAGE MEASUREMENTS	57
5.2(a)	Under Sunlight	57
5.2(b)	Simulated Sunlight	58
5.2(c)	Dark Characteristics	59
5.3	PHOTORESONSE	59
5.4	CELL DU-35	60
5.5	DISCUSSION OF RESULTS	61
6	CAPACITANCE MEASUREMENTS	75
6.1	INTRODUCTION	75
6.2	MEASUREMENT SETTINGS	75
6.3	VARIATION WITH FREQUENCY	76
6.4	CELL 35 - VARIATION WITH BIAS AND FREQUENCY	76
6.5	MOTT-SCHOTTKY PLOTS	77
6.6	DISCUSSION	77
7	GENERAL DISCUSSION AND CONCLUSIONS	83
	REFERENCES	87

Chapter 1

Introduction

The chalcopyrite semiconductor CuInSe_2 is an important material for the absorber layer of a thin film photovoltaic solar cell because of its high optical absorption coefficient in the main part of the solar spectrum and its good chemical stability. Quaternary and pentenary chalcopyrite alloys based on this compound have shown even better photovoltaic performance than the ternary. Thus, for instance, a cell with the basic layer structure $\text{Cu}(\text{In}_{1-x}\text{Ga}_x)\text{Se}_2\text{-CdS-ZnO}$ fabricated at the National Renewable Energy Laboratory (NREL) in Golden, Colorado, has yielded a solar conversion efficiency of 19.2 % [1.1] and there is hope, with sufficient research, that 20 % can be reached. While the main advantage of this chalcopyrite semiconductor is in the lower material cost in fabrication because only thin films are needed to capture and convert most of the incoming photons into charge carriers, the cells made from it have also shown remarkable radiation hardness [1.2], so that they could be exploited in outer space applications. Furthermore, the devices in panel form have shown excellent stability under continuous illumination .

The main interest in the photovoltaic community, working with the chalcopyrite alloys, has been in thin film polycrystalline material, such as $\text{Cu}(\text{In}_{1-x}\text{Ga}_x)\text{Se}_2$ (CIGS), where great progress has been made. However, the present study is on *monocrystalline* CuInSe_2 (CIS) and cells made from it. The ternary material was chosen, in the first instance, because it is simpler to prepare, without consideration of the effects of gradients in the

spacial distribution of a fourth element [1.3], such as gallium. This simplification is especially important in working with nonstoichiometric ternary material. The monocrystalline form was employed to avoid effects associated with grain boundaries. One of these seems to be that single crystal cells are adversely affected by oxygen [1.4], in contrast to its beneficial effect on polycrystalline thin film cells.

By comparison to the progress made in polycrystalline thin film cells, the history of cells with monocrystalline absorber layers has been slow, with essentially the same conversion efficiency of about 12 % (with an antireflection coating) over the last quarter of a century. The area of the cell of Shay, Wagner and Kasper in 1975 [1.5] was only 0.8 mm², and better results were obtained only on very small area devices prepared by Kazmerski and Sheldon [1.6] and by Arya, et al. [1.7]. However, the area of the cell fabricated by Yip and Shih [1.8] of this laboratory in 1993 was some 8 mm², an order of magnitude larger. This situation is, of course, quite different from the case with silicon, where the highest efficiency cells use this element in monocrystalline form and where the performance in polycrystalline devices is lower [1.9]. The reason for this is the longer optical absorption depth (from the lower absorption coefficient α) and larger minority diffusion length in silicon compared to CuInSe₂. Thus, in CIS, making the crystal size greater than $1/\alpha$ is not likely to increase the photocurrent substantially. Nevertheless, in principle, a CIS cell using monocrystalline material should eventually, it would seem, show a slightly higher efficiency than a polycrystalline device. As a step in this direction, the present work aims to explore this possibility, as well as to determine factors which could help in improving the chalcopyrite-based cell generally.

It must be realized in growing a single crystal of CuInSe₂ from its starting elements

of copper, indium and selenium, that direct synthesis in an open crucible will not work, since it would result in the complete loss of the selenium due to its much higher vapour pressure than that of the other two elements. Hence, in growth from the melt, the elements must be enclosed in a sealed ampoule, able to withstand the vapour pressure of selenium of some 40 atmospheres at 1,100 °C. This was done in the present studies using a thick-walled quartz ampoule. A comprehensive history of the growth of CuInSe_2 crystals by the Bridgman method is described by Champness [1.10].

The first part of this work consisted of the growth of CIS ingots using a vertical Bridgman method. The techniques used were based on those developed previously in this laboratory by Ziad A. Shukri [1.11] and Galaly I. Ahmad [1.12], whereby a single ampoule was used for both compound synthesis and subsequent crystal growth of the ingot in a vertical Bridgman furnace. Furthermore, an inner coating of flamed-in boron nitride was used to eliminate unwanted adhesion of the ingot to the ampoule wall and to minimize the formation of voids in the ingot. These procedures have resulted in microcrack-free CIS material more uniform in composition and conductivity than produced in other laboratories. Ingots were prepared from both stoichiometric and nonstoichiometric melt compositions. This work on ingot preparation is described fully in chapter 3.

Prior to this, in chapter 2, some photovoltaic basics are presented. One is a calculation justifying quantitatively the use of thin films for material with a high optical absorption coefficient, such as CuInSe_2 . The other useful concept treated in the chapter is the simple equivalent circuit of a photovoltaic cell and the possible use of gradients in the illuminated current-voltage characteristics to estimate shunt and series resistances in imperfect cells.

The second main part of this work consisted of the fabrication of a photovoltaic cell using a wafer of p-type CuInSe_2 cut from the Bridgman-grown material as the absorbing substrate. Several such devices were prepared having the layer structure $\text{Au-CuInSe}_2\text{-CdS-ZnO-In}$. The thin CdS buffer layer was put down by a chemical bath dipping process and the ZnO layer was deposited by rf sputtering. Gold was evaporated on the back of the wafer and contact stripes of indium were evaporated on the ZnO area. A schematic cross-sectional view of a cell is shown in Figure 1.1. The cell fabrication processes are described in detail in chapter 4.

Measurements on the cells, mostly under illumination, are described in chapter 5. Current-voltage readings were taken in darkness and under illumination from a solar simulator and directly under full sunlight in Montreal. Photoresponse measurements were also taken on the cells. In the case of the best cell fabricated, its characteristics were also measured at NREL.

Chapter 6 describes capacitance measurements made on the cells as a function of voltage bias and frequency. From these, Mott-Schottky plots were obtained. Finally in chapter 7, the results of the study are reviewed and discussed.

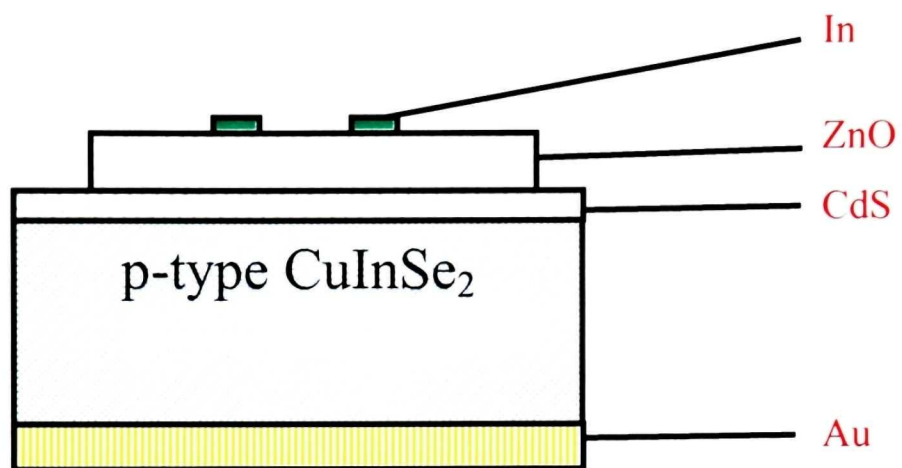


Figure 1.1 Schematic of the fabricated monocrystalline CuInSe_2 photovoltaic cell.

Chapter 2

Some Photovoltaic Fundamentals

2.1 INTRODUCTION

The theoretical basis of photovoltaic action is described in many textbooks, such as H.J. Hovel [2.1], M.A. Green [2.2] and M.D. Archer [2.3]. Hence the full treatment of the phenomenon will not be repeated here. However, it is useful to treat certain features of photovoltaic cell analysis which are relevant to the present work, so that they can be conveniently referred to in later parts of this thesis. Accordingly, in this chapter, a calculation will be presented of the variation of photocurrent with optical penetration depth. It gives the rationale for the use of high optical absorption coefficient material, such as CuInSe_2 , for the absorber layer in thin film solar cells. A second topic, which will be briefly reviewed here, is the application of a simple equivalent circuit of a photovoltaic cell, since this is helpful in understanding the current-voltage characteristics under illumination.

2.2 MAXIMUM PHOTOCURRENT

Consider the simplified n^+p cell in Figure 2.1. Suppose light of wavelength λ and irradiance E_0 in $\text{watt/cm}^2/\mu\text{m}$ is incident on the n^+ surface, where fraction R is reflected. If the light absorbed in the thin n^+ layer is neglected, the light energy per second entering the p -region is $E_0(1 - R)$. If $\alpha(\lambda)$ is the optical absorption coefficient at a wavelength λ , then the

light intensity at a distance x into the p-region is reduced to $E_o(1 - R)\exp(-\alpha x)$. Hence the amount of energy absorbed per second in the region of depth x is:

$$E_o(1 - R) - E_o(1 - R)e^{-\alpha x} = E_o(1 - R)(1 - e^{-\alpha x})$$

Now the number of photons absorbed per second is this quantity divided by $h\nu$, where h is Planck's constant, $\nu = c/\lambda$ is the optical frequency and c is the velocity of light. If each photon absorbed produces one electron-hole pair, equivalent to one electronic charge q (i.e. there is a quantum efficiency of unity), then the contribution to electric current per unit area Δj for a wavelength interval $\Delta\lambda$ is:

$$\Delta j = \frac{qE_o}{hc}(1 - R)(1 - e^{-\alpha x})\lambda \cdot \Delta\lambda$$

Hence, for an optical source distribution between λ_1 and λ_2 , the photocurrent per unit area j_{ph} would be given by

$$j_{ph} = \frac{q}{hc} \int_{\lambda_1}^{\lambda_2} E_o(\lambda)[1 - R(\lambda)][1 - e^{-\alpha(\lambda) \cdot x}] \lambda \cdot d\lambda \quad (2.1)$$

2.2(a) Wavelength Limitations

Photons with energies below the optical energy gap E_G are not able to create electron-hole pairs, so that their quantum efficiency is zero. Thus, $j_{ph} = 0$ for $h\nu < E_G$, so that the upper limit in the integral of equation (2.1) would be $\lambda_2 = hc/E_G$. The lower bound could be given by the wavelength for absorption in the n^+ window layer but, in any case, if the sun's spectrum is used, the irradiance for wavelengths less than $0.3 \mu\text{m}$ is very small, so that the limit $\lambda_1 = 0.3 \mu\text{m}$ could be used, yielding:

$$j_{ph} = \frac{q}{hc} \int_{0.3}^{\frac{hc}{E_G}} E_o(\lambda)[1 - R(\lambda)][1 - e^{-\alpha(\lambda) \cdot x}] \lambda \cdot d\lambda \quad . \quad (2.2)$$

2.2(b) Special Simplified Case

Suppose for simplicity that E_o and α are independent of wavelength between $\lambda_1=0.3\mu\text{m}$ and $\lambda_2=1.3\mu\text{m}$, where $E_o = 90 \text{ mW/cm}^2/\mu\text{m}$, $\alpha = 10^4 \text{ cm}^{-1}$, $R = 0$ and $x = 1\mu\text{m}$. Then from equation (2.2)

$$\begin{aligned} j_{ph} &= \frac{qE_o}{hc} (1 - e^{-\alpha x}) \int_{0.3}^{1.3} \lambda \cdot d\lambda \\ &= \frac{1.6 \times 10^{-19} \text{ coul} \cdot 90 \text{ mW/cm}^2/\mu\text{m}}{6.626 \times 10^{-34} \text{ js} \cdot 3 \times 10^{10} \text{ cm/s}} \left[1 - e^{\left(-10^4 \cdot 10^{-4}\right)} \right] \left(\frac{\lambda^2}{2} \right)_{0.3}^{1.3} (\mu\text{m})^2 \\ &= 36.6 \text{ mA/cm}^2 \end{aligned}$$

For infinite depth, that is $x = \infty$, instead of $1\mu\text{m}$, this current would be increased by the factor $1/(1 - e^{-1}) = 1.58$, yielding $j_{ph} = 58 \text{ mA/cm}^2$.

2.2(c) Numerical Integration for CuInSe₂

Instead of algebraic integration in equation (2.2), the calculation of current can be done numerically by dividing the solar spectrum into wavelength intervals of $\Delta\lambda$ and adding up the contributions from each wavelength strip. In this process, equation (2.2) is replaced for $R = 0$ by:

$$j_{ph} = \frac{q}{hc} \sum_{i=0.3}^{i=1.3} E_{oi} \lambda_i [1 - e^{-\alpha_i x}] \lambda_i \cdot \Delta\lambda \quad , \quad (2.3)$$

where the summation is over each i -value. In the present case, this numerical integration has been done for CuInSe_2 using the AMG 1.5 solar spectrum shown in Figure 2.2 [2.4] by using strips of width $\Delta\lambda = 0.1 \mu\text{m}$ between 0.3 and $1.3 \mu\text{m}$. An average value of E_0 in $\text{mW/cm}^2/\mu\text{m}$ from Figure 2.2 in each strip was multiplied by the appropriate value of $[1 - \exp(-\alpha x)]$ using an α -value at each wavelength, obtained from the literature [2.5]. Each of these E_0 values was in turn multiplied by the mid-strip wavelength value and $\Delta\lambda$ to give the appropriate product, all of which were added up to give the current for the particular chosen value of penetration depth x , assuming the surface reflectance R to be zero. Table 2.1 illustrates this calculation for the case of $x = 0.5 \mu\text{m}$, resulting in the photocurrent of 41.85 mA/cm^2 for this optical path length.

In this way, calculations were done for x -distances up to $2 \mu\text{m}$ into CuInSe_2 , yielding the plot of variation of photocurrent with optical penetration depth in Figure 2.3. While the accuracy of this plot depends on that of the E_0 and α -values used, it is clear that at a CuInSe_2 thickness of $2 \mu\text{m}$ for instance, the short circuit current would be 98% ($= 49.8/50.6$) of its maximum value. Thus, this material is a true candidate for a thin film solar cell.

2.3 SIMPLE EQUIVALENT CIRCUIT OF CELL

2.3(a) Current-voltage Relation

A simple equivalent circuit of a junction photovoltaic cell is that shown in Figure 2.4. It consists of a current generator, yielding a photocurrent I_{ph} . Across this, in parallel, is a diode and a shunt resistance R_{sh} , followed by a series resistance R_s . The diode current I_D is given by

$$I_D = I_o (e^{\frac{qV_D}{nkT}} - 1) \quad , \quad (2.4)$$

where V_D is the voltage across the diode, n is the diode ideality factor, k is Boltzmann's constant, T is absolute temperature and I_o is the diode reverse saturation current.

Using the current sign convention for diodes (positive current in the diode forward direction), the current I entering terminal A from the external load R_L is given by

$$I = I_o [e^{\frac{q(V - IR_s)}{nkT}} - 1] + \frac{V - IR_s}{R_{sh}} - I_{ph} \quad . \quad (2.5)$$

Hence, in an ideal cell where $R_s = 0$ and $R_{sh} = \infty$, the short circuit current I_{sc} (at $V = 0$) would be given by $I_{sc} = -I_{ph}$ and the open circuit voltage V_{oc} (at $I = 0$) for $\frac{qV_{oc}}{nkT} \gg 1$ by

$$V_{oc} = \frac{nkT}{q} \ln\left(\frac{I_{ph}}{I_o}\right) \quad . \quad (2.6)$$

For a non-ideal cell, where R_s and $1/R_{sh}$ are greater than zero

$$I_{ph} = I_o [e^{\frac{qV_{oc}}{nkT}} - 1] + \frac{V_{oc}}{R_{sh}} \quad .$$

So that if $V_{oc} \gg \frac{nkT}{q}$, then

$$V_{oc} = \frac{nkT}{q} \ln\left(\frac{I_{ph} - \frac{V_{oc}}{R_{sh}}}{I_o}\right) \quad .$$

2.3(b) I-V Gradients

A schematic current-voltage characteristic for a cell under illumination is shown in Figure 2.5. From this diagram, the gradients at short circuit and open circuit conditions can be useful. Thus, from equation (2.5), it can readily be shown by differentiation that:

$$R_{sh} = \left[\frac{\left(\frac{dI}{dV}\right)_{sc}}{1 - R_s \left(\frac{dI}{dV}\right)_{sc}} - I_o \frac{q}{nkT} e^{-\frac{qI_{sc}R_s}{nkT}} \right]^{-1} \quad (2.7)$$

and

$$R_s = 1 / \left[\left(\frac{dI}{dV}\right)_{oc} - \left[\frac{qI_o}{nkT} e^{\frac{qV_{oc}}{nkT}} + \frac{1}{R_{sh}} \right] \right]^{-1}, \quad (2.8)$$

where $\left(\frac{dI}{dV}\right)_{sc}$ and $\left(\frac{dI}{dV}\right)_{oc}$ are the gradients at $V=0$ and $I=0$ respectively. If $R_s=0$, then

from equation (2.7), R_{sh} is given by

$$R_{sh} = \left[\left(\frac{dI}{dV}\right)_{sc} - I_o \frac{q}{nkT} \right]^{-1},$$

which if

$$I_o \frac{q}{nkT} \ll \left(\frac{dI}{dV}\right)_{sc}, \quad (2.9)$$

becomes

$$R_{sh} = 1 / \left(\frac{dI}{dV}\right)_{sc}. \quad (2.10)$$

If $R_{sh}=\infty$, then from equation (2.8), R_s is given by

$$R_s = 1 / \left[\left(\frac{dI}{dV}\right)_{oc} - \frac{nkT}{qI_o} e^{-\frac{qV_{oc}}{nkT}} \right],$$

and if

$$\frac{nkT}{qI_o} e^{-\frac{qV_{oc}}{nkT}} \ll 1 / \left(\frac{dI}{dV}\right)_{oc}, \quad (2.11)$$

this becomes
$$R_s = 1 / \left(\frac{dI}{dV} \right)_{oc} . \quad (2.12)$$

It is helpful to determine what inequalities (2.9) and (2.11) mean for the type of CuInSe₂ I-V characteristics in this thesis. Thus, assuming n=2 and working with current densities j (amp/cm²) and area resistances R_{sh}^* and R_s^* (Ωcm^2) with $j_0 = I_0/A = 2 \times 10^{-6}$ A/cm², where A is the cell area, inequality (2.9) becomes

$$R_{sh}^* \ll 2.6 \times 10^4 \Omega\text{cm}^2 ,$$

and if V_{oc} is taken as 0.5 volt, then inequality (2.11) becomes

$$R_s^* \gg 1.6 \Omega\text{cm}^2 .$$

Hence, the I-V gradients, at short and open circuit conditions, only reflect the shunt and series resistances respectively when the cell performance is less than perfect.

Table 2.1
Typical Calculation of Photocurrent Variation with Depth in CuInSe₂
x=0.5 μm $\Delta\lambda=0.1 \mu\text{m}$ Wavelength range $\lambda=0.3$ to $1.3 \mu\text{m}$ R=0

λ (μm)	α (cm^{-1})	αx	$1 - \exp(-\alpha x)$	E_o ($\text{mW}/\text{cm}^2/\mu\text{m}$)	$\frac{qE_o\lambda\Delta\lambda}{hc}$ (mA/cm^2)	$\frac{qE_o\lambda\Delta\lambda}{hc} [1 - \exp(-\alpha x)]$ (mA/cm^2)
0.35	10^5	5	0.993	45	1.27	1.26
0.45	10^5	5	0.993	130	4.71	4.68
0.55	7.5×10^4	3.75	0.976	155	6.86	6.70
0.65	7×10^4	3.5	0.970	140	7.32	7.10
0.75	5×10^4	2.5	0.918	110	6.64	6.10
0.85	4.5×10^4	2.25	0.895	90	6.16	5.51
0.95	3×10^4	1.5	0.777	60	4.59	3.57
1.05	2×10^4	1.0	0.632	65	5.49	3.47
1.15	1.4×10^4	0.7	0.503	35	3.24	1.63
1.25	1.1×10^4	0.55	0.423	43	4.33	1.83
						Sum=41.85 mA/cm^2

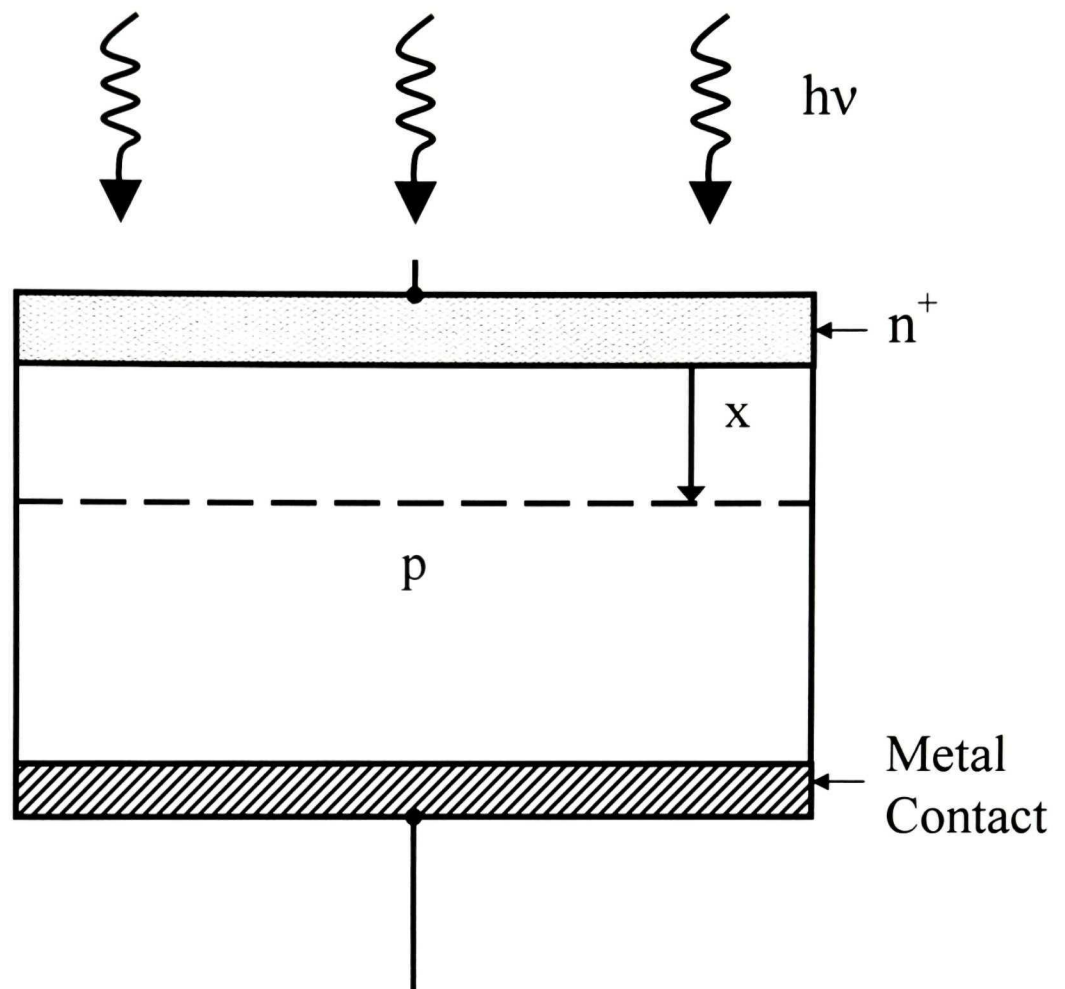


Figure 2.1 Schematic of illuminated n^+p cell.

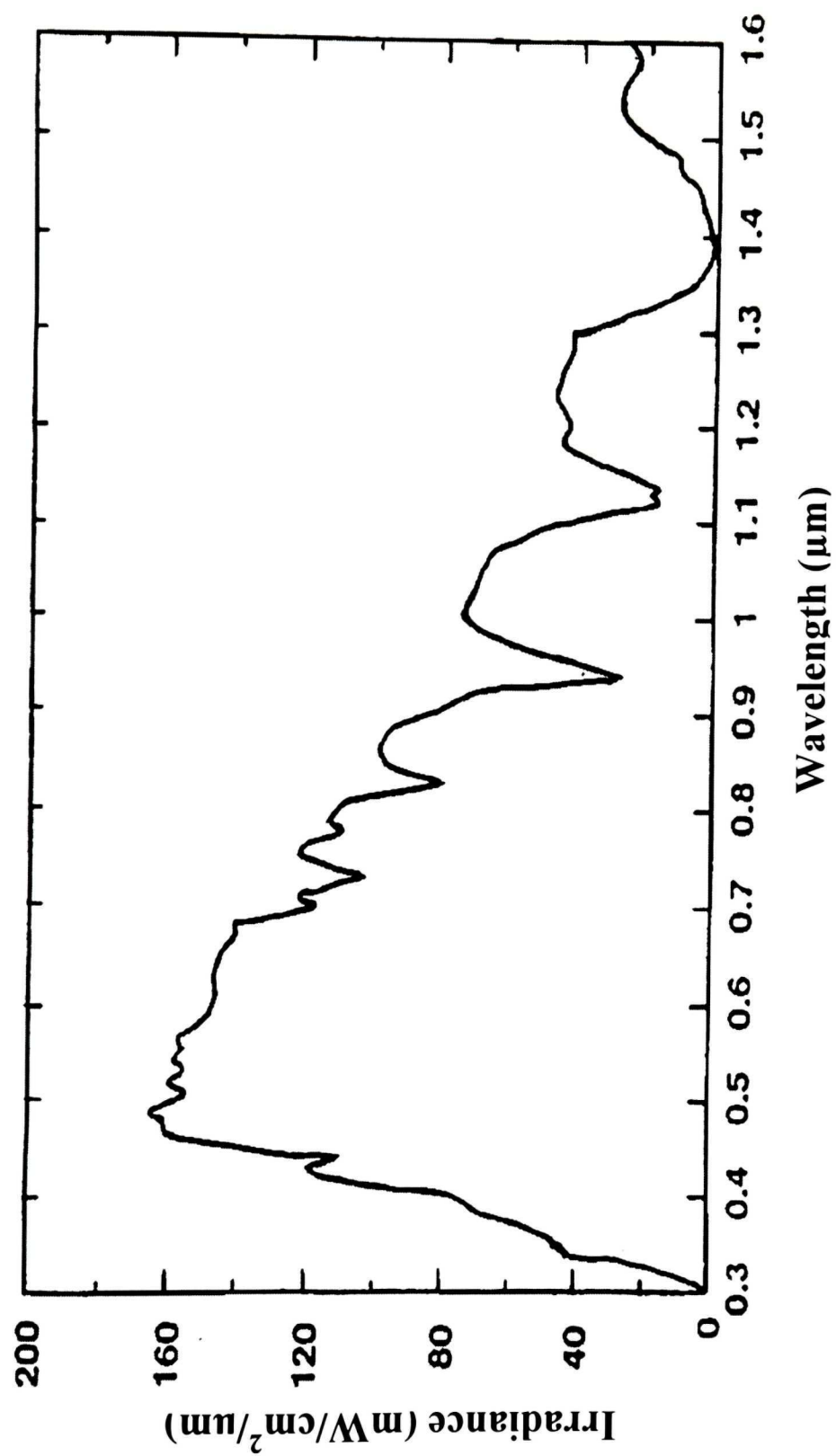


Figure 2.2 Air Mass 1.5 Global spectrum (100 mW/cm²).

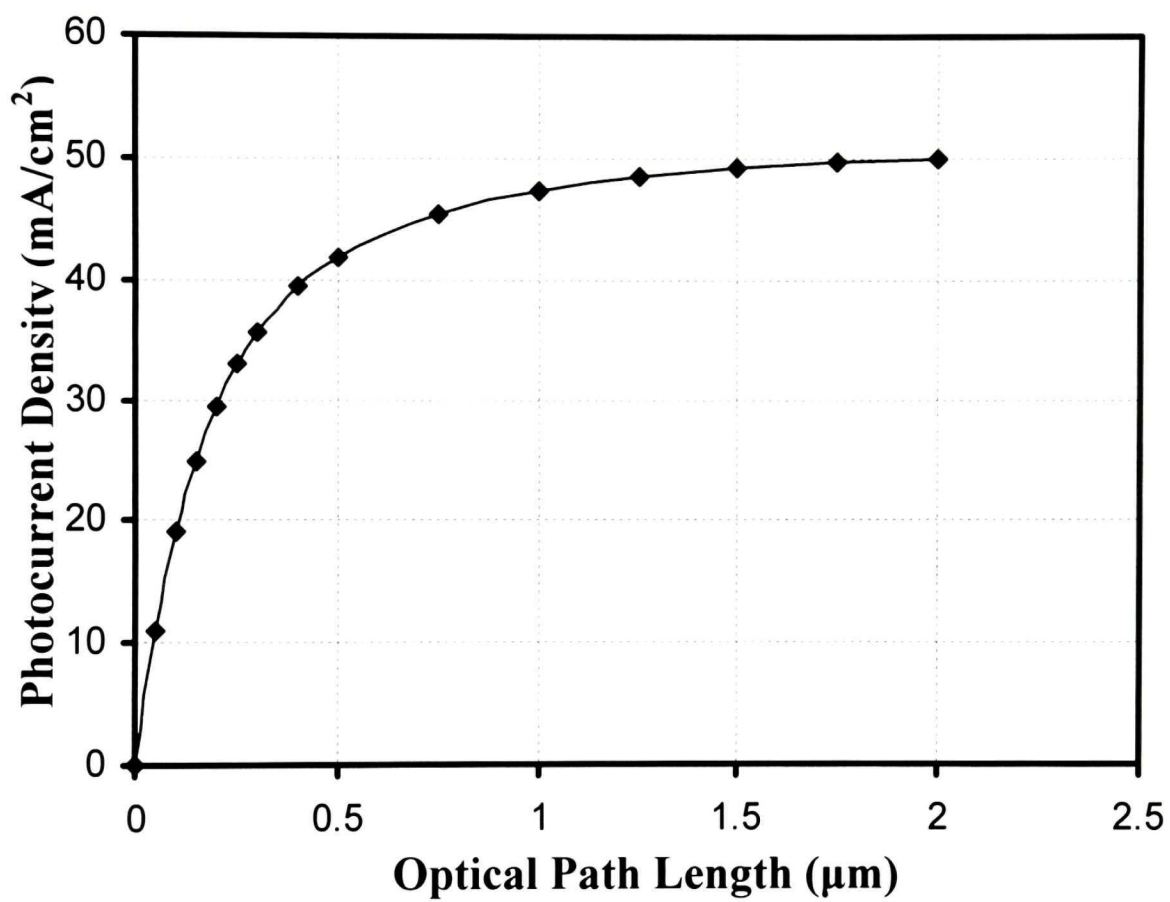


Figure 2.3 Variation of photon current with optical penetration depth.

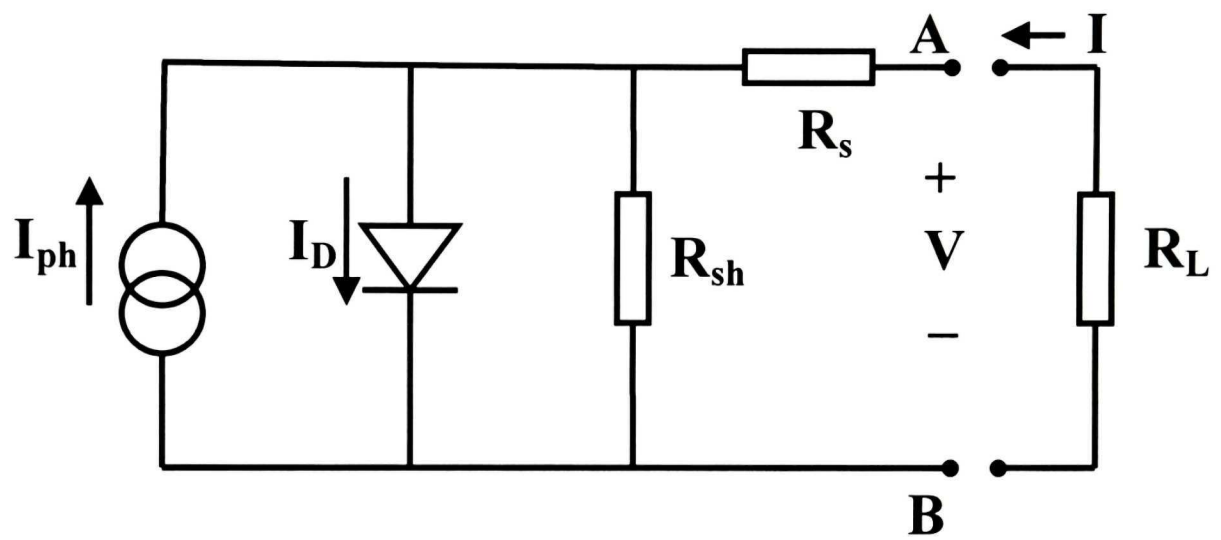


Figure 2.4 Simple equivalent circuit of a photovoltaic cell.

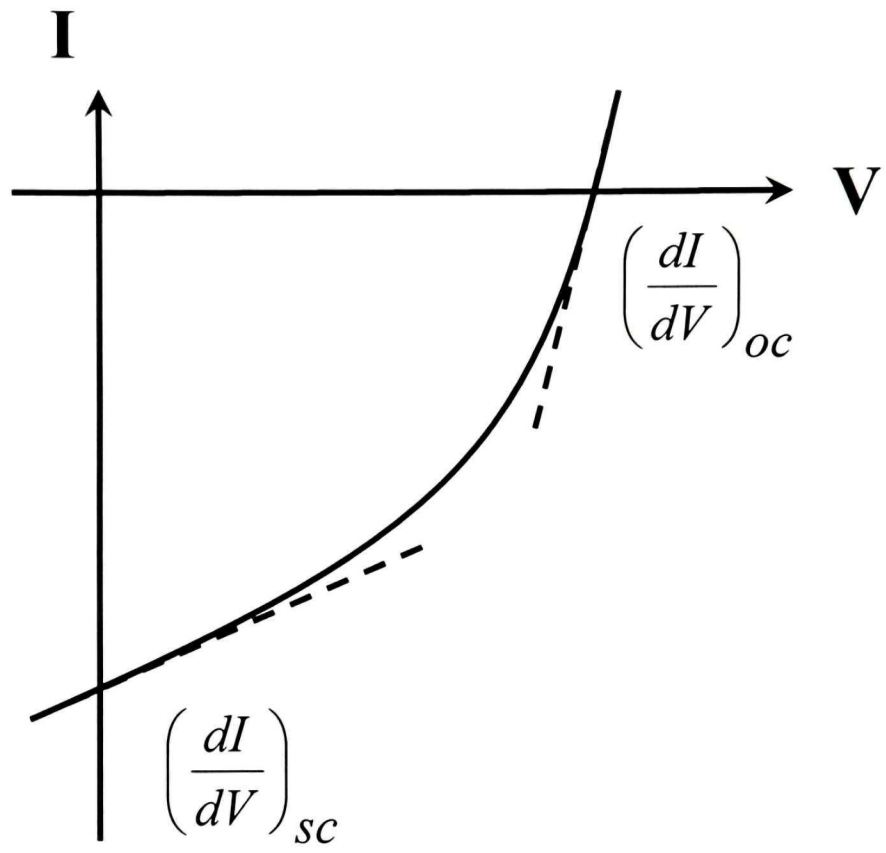


Figure 2.5 Current-voltage characteristic of a nonideal photovoltaic cell under illumination.

Chapter 3

Bridgman Growth of CuInSe_2

3.1 INTRODUCTION

As mentioned in chapter 1 of this thesis, the first part of these studies involved the growth of monocrystalline CuInSe_2 and the present chapter describes specifically the work of preparing ingots of this ternary compound. Using a vertical Bridgman method, the techniques employed followed those developed by Z.A. Shukri [1.11] and G.I. Ahmad [1.12] using the unique features of employing one ampoule for both compound synthesis and crystal growth and using a flamed-in boron nitride coating on the inner wall of the quartz ampoule containing the original elements. Ingots were prepared from stoichiometric proportions of the elements in the melt, as well as from specific nonstoichiometric proportions.

Before details of the ingot preparation are presented in this chapter, it may be helpful to first give a brief outline of the procedures involved. First the quartz ampoule was prepared and thoroughly cleaned. Next high purity pellets of the elements copper, indium and selenium, after etching, were weighed out in the appropriate atomic proportions and introduced into the ampoule, which was then pumped out and sealed off. The ampoule was then placed in a furnace and heated until the reaction between the In and the Se was completed, following which the ampoule was removed and a long quartz rod was attached to it. Then the ampoule, with its attached rod, was inserted in a vertical Bridgman furnace,

consisting of two heater sections. The temperature was raised so that synthesis of the ternary compound could take place and then the ampoule was maintained at a temperature above the melting point of CuInSe_2 to ensure homogeneity. Following this, the ampoule was slowly lowered through the temperature gradient in the furnace to the lower cooler section, where the motion was stopped and the ampoule allowed to cool slowly to room temperature. It was then removed from the furnace and broken open to obtain the ingot, which was examined visually and by four point probe and hot probe for respectively electrical resistivity and approximate thermoelectric power determination.

3.2 AMPOULE PREPARATION

3.2(a) Ampoule Formation

The ampoule used was made from quartz tubing with an outer diameter of 16 mm and an inner diameter of 12 mm. The wall thickness of 2 mm was necessary to withstand the high vapour pressure of the selenium in the ampoule at temperatures above the melting point of CuInSe_2 - amounting to some 40 atmospheres at 1,100 °C. To shape the ampoule with a pointed tip for enhancing crystal growth, it was necessary to use an oxygen-hydrogen flame because of the high softening temperature of the quartz. The conical tip was obtained by uniformly heating the quartz tube and drawing it out to a smaller diameter. In this procedure, the key skill is to thin the diameter little-by-little, rotating the tube at the same time. Following this, the diameter of the tube, well away from the tip, was reduced by thinning down to enable the eventual sealing off process to be easier, keeping the inner diameter large enough for the pellets to pass through. At this stage, the usual length from the tip to the wide open end was more than 30 cm .

3.2(b) Ampoule Cleaning

The ampoule was cleaned by first pouring in a 1:1 mixture of hydrochloric (HCl) and nitric (HNO_3) acids and leaving it for 10 to 30 hours to remove impurities, followed by a rinse in de-ionized (DI) water. Then acetone was introduced for a similar period to remove organic contaminants with a final rinse in DI water.

3.2(c) Boron Nitride Coating

A coating of flamed-in boron nitride (BN) was reported by Z.A.Shukri [1.11] and by Shukri, Champness and Shih [3.1] to inhibit adherence of the ingot to the ampoule walls. This procedure was therefore also carried out by the author in the following way. About 2 grams of boron nitride white powder (from Johnson Matthey Ltd.) of nominal purity 99.5 % was mixed with 5 to 10 ml of acetone in a small beaker and agitated to obtain a suspension. After this, the mixture was quickly transferred to the ampoule, which was given manual agitation for 2 to 3 minutes. When the excess quantity was poured out, some of it adhered to the inner wall of the ampoule. The mixture in the region of the ampoule where BN was not wanted, was washed away with DI water, leaving a uniform coating of acetone-wet BN in the region of the ampoule near the tip. Next the ampoule was heated in a small oven to evaporate off the remaining acetone and then the coated region was heated intensively in an oxy-hydrogen flame until the BN was absorbed into the quartz, so that it was again transparent. In some cases the procedure was repeated to obtain a second coating.

3.3 COMPOUND SYNTHESIS

3.3(a) Pellet Etching

The starting elements: copper, indium and selenium were in pellet form, with a diameter of 3 to 5 mm and of nominal 99.999 % purity. Because of surface oxidation and contamination from storage, it was necessary to etch away any surface film on the pellets before use. The copper pellets were etched in dilute nitric acid (DI water to acid volume ratio of 10:1) for 2 to 3 minutes, while the indium and selenium pellets were separately etched in dilute hydrochloric acid (water to acid ratio 10:1) for a similar time. It was found that excessive etching of the indium pellets caused them to stick together, which was undesirable for the weighing step. The etched pellets were then weighed out in the appropriate atomic proportions, which, for example, for the first five growth runs was 1:1:2 for Cu, In and Se respectively. The total weight of the pellet charge was from 9 to 18 grams.

3.3(b) Ampoule Pumping and Sealing

After weighing, the etched pellets were introduced into the BN-coated ampoule-tube through the open end. In filling the tube, the Se pellets were first introduced, followed by the In and then the Cu pellets. Having the copper on the top of the ampoule in a vertical position was helpful during the hot sealing off process because of the higher melting point of this element (1083°C) compared to that of indium (156°C) and selenium (217°C). The sealing off was done by first attaching the open end of the ampoule tube to a pumping system, consisting of a mechanical and an oil diffusion pump, and pumping down to a pressure of about 10^{-6} Torr. Then heat from an oxy-hydrogen flame was applied to the previously thinned down region of the ampoule tube, usually arranged to be some 10 cm above the charged pellets, keeping, at the same time, the tip end cool with wet paper. With

continued heating and pumping, the quartz in the thinned down region softens and eventually collapses together, sealing off the lower charged part of the tube to form a closed ampoule. This was then detached from the rest of the tube ready for the next step (Figure 3.1).

3.3(c) Pre-reaction of the Charge

The sealed ampoule, containing its pellet charge, was then placed in a benchtop brick furnace, where the temperature was slowly raised at about $1^{\circ}\text{C}/\text{min}$ to a temperature of 300°C . This was to allow the lower melting point elements indium and selenium to react together and, since this reaction is exothermic, a slow heating rate was necessary to reduce the possibility of an ampoule explosion from the resulting exothermic heat generated within. On reaching 300°C , the temperature was maintained at this value for more than 10 hours, after which the ampoule was removed from the furnace and allowed to cool down.

3.4 BRIDGMAN GROWTH

3.4(a) Temperature Soak

A quartz rod, some 60 cm in length was first attached to the sealed off end of the ampoule. This was inserted in the vertical tube of a two-section Bridgman furnace, shown schematically in Figure 3.2, with the non-ampoule end of the rod connected to the mechanical lowering system of the equipment. The ampoule was next positioned in the middle of the top heater section of the furnace and the temperature was raised at the rate of $5^{\circ}\text{C}/\text{min}$ up to $1,100^{\circ}\text{C}$, about 100 degrees above the melting point of CuInSe_2 of 986°C . It was then maintained at this temperature for more than 24 hours, during which time the

ampoule was frequently removed quickly from the furnace and given a manual shaking to ensure thorough mixing and homogeneity of the melt and then returned to the furnace (row 7 of Table 3.1). The furnace temperatures were measured using two thermocouples, one positioned in the middle of the top heater section (T1 in Figure 3.2) and another located in the middle of the lower section (T2 in Figure 3.2) .

3.4(b) Ampoule Lowering

At the end of the temperature soak period, the lowering procedure was begun to initiate the crystal growth process. With the ampoule starting at a position in the top furnace about 6 cm above the baffle (Figure 3.2), the temperature of the lower furnace section was raised to about 700° C and the motor, operating the lowering of the quartz rod and ampoule rod, was switched on. With a rate of 4 to 6 mm/hour, the ampoule was lowered slowly through the top heater section, through the insulating baffle, into the lower heater section. With the ampoule well into the lower section, the lowering was stopped and the ampoule was allowed to cool from 700°C to room temperature at a controlled rate of 15 to 30°C/hour . This slow cooling of the solid ingot within the ampoule is necessary [1.11] to reduce internal stresses in the material. The ampoule was then removed from the Bridgman furnace and broken open to retrieve the ingot. If the boron nitride treatment was properly carried out, the ingot showed no adherence to the inner ampoule wall. This was the case for the ingots prepared in this work, except for an instance, where air entered the ampoule via a crack (ingot DH-B05 in Table 3.1). The total lowering process lasted usually from 48 to 72 hours.

3.4(c) Temperature Profile of Bridgman Furnace

Prior to the growth runs, the temperature profile along the central tube of the two-section Bridgman furnace was determined using a movable type K thermocouple (consisting of alloys of Ni-Cr and Ni-Al), with the top middle section set at 1,100°C (as determined by the top fixed position thermocouple T1) and the bottom section set at 700°C (T2). Between the two furnace sections was an insulating baffle consisting of a circular plate of asbestos, with a thickness of about 3.5 cm. The temperature profile, so determined, is shown in Figure 3.3, where it is seen that the largest temperature change takes place just below the baffle region.

3.4(d) Specific Growth Run Conditions

Some 14 ingots of the ternary chalcopyrite were prepared, where the details of the growth runs are given in Table 3.1. The first two runs must be considered as “training runs”, since their ingots (DH-B01 and DH-B02) were unsatisfactory with only small crystallites. For the other 12 runs, the following synthesis and growth conditions are noted. The time allowed for the In - Se chemical reaction was 9 hours or more and that for the soak time of the melt at 1,100°C was more than 30 hours. The ampoule lowering rates were generally about 5 mm/hr and the ingot cooling rates for the ingot in the lower section of the Bridgman furnace were less than 50 °C/hr. Among the 12 runs, it is noted that 5 were prepared with stoichiometric proportions of the starting elements (ingots DH-B03, 04, 05, 13, 14), 5 were with excess copper (ingots DH-B08, 09, 10, 11 and 12), 1 with excess selenium (DH-B06) and 1 with a deficiency of selenium (DH-B07).

3.5 RESULTS

3.5(a) Crystallinity of Ingots

After growth, each ingot was first inspected visually for external features and any small pieces of it, broken away from the fracturing of the ampoule, were examined under an optical microscope. Except for ingots DH-B01 and DH-B02, the remaining 12 ingots consisted of many monocrystals, each with a minimum dimension of 2 mm. Their presence was very clear from the many observed $\{112\}$ and $\{101\}$ cleavage facets and $\{112\}$ twin lines [3.2]. Figure 3.4 shows a cleavage plane and Figure 3.5 shows clear twin lines. Arising from the boron nitride action, the ingots contained either no or only a few cavities. Apart from this, the curved surface of each ingot, molded by the inner wall of the ampoule, had few special features. However, when a small external cavity was present, it represented an excellent opportunity to observe within it crystal growth free of ampoule wall restriction. Thus, Figure 3.6 shows, within such a cavity, features in the form of equilateral triangles, which represent growth facets on a $\{112\}$ plane. Such facets were approximately parallel to the ingot axis, so that the normal to the $\{112\}$ plane (ie. in a $\langle 221 \rangle$ direction) would be perpendicular to this axis. This is not necessarily contrary to an earlier observation [3.3] that the growth direction along the ingot axis is $\langle 221 \rangle$, since the angle between adjacent $\langle 221 \rangle$ directions is 70.53° , which approaches a right angle in magnitude.

3.5(b) Electrical Evaluation of Ingots

In many cases, slices were abrasively cut across each ingot with thicknesses of 1-3 mm and polished abrasively. Then four point probe [3.4] and hot probe[3.5] tests were made on each of the two faces of every wafer, keeping the voltage to the hot point heater the

same (30 volt) from one test to the next. The results are summarized in Tables 3.2 and 3.3. Powder X-ray diffraction patterns were also obtained on some samples. Schematic diagrams of the four point probe and hot probe used are shown respectively in Figures 3.7 and 3.8.

(i) Ingots with selenium nonstoichiometry

Table 3.2 gives results for 5 ingots, including one prepared with an excess of selenium, corresponding to a melt composition of $\text{CuInSe}_{2.2}$ and another with a deficiency of this element corresponding to a composition of $\text{CuInSe}_{1.8}$. The former was confirmed by hot probe to be p-type and the latter n-type. The n-type material was especially interesting, since the end of the ingot, that is the last zone to freeze, was distinctly different from the rest of the material. Here, extra phases in globular form were visible, as indicated in Figure 3.9(a). By contrast, no such phases were observed in the rest of the ingot (Figure 3.9(b)). X-ray diffraction of powdered material from the end region (not shown) indicated the presence of InSe . For a similar preparation of composition $\text{CuInSe}_{1.7}$, Shukri et al. [3.6] also found Cu_7In_4 and Cu_9In_4 in this last zone but, so far, these binaries have not been confirmed by X-ray diffraction in the present work. Hot probing in this region showed lower thermoelectric voltages than in the rest of the n-type ingot, suggesting a higher electron concentration in the last zone to freeze. The p-type ingot with excess selenium, corresponding to the melt composition $\text{CuInSe}_{2.2}$ (column 2 in Table 3.2) was expected, from previous work, to have a higher hole concentration than that in the stoichiometric ingots (column 3 in Table 3.2). However the four point probe and hot probe values for the middle of the ingot indicated little change. Moreover, the resistivity at the end of the excess

selenium ingot was reduced. The stoichiometrically prepared ingot of column 5 in Table 3.2 was found to be darker in appearance than usual. This arose from surface oxidation, due to a crack in the ampoule, which occurred during the Bridgman growth and also caused the middle of the ingot to be n-type by partial loss of selenium via the crack. Thus, any oxygen present, acting as an acceptor [3.7], did not manage to keep the material p-type in this region, although the ingot end was still strongly p-type.

(ii) Ingots with copper excess

Ingots were prepared with increasing proportions of copper, corresponding to melt compositions of CuInSe_2 , $\text{Cu}_{1.1}\text{InSe}_2$, $\text{Cu}_{1.2}\text{InSe}_2$, and $\text{Cu}_{1.3}\text{InSe}_2$, as indicated in Table 3.3. Except for the stoichiometrically prepared ingots of column 2, precipitated copper was freely visible on the end surface of each copper excess ingot; that is on the last surface to freeze in the growth process. This precipitated copper was in the form of a fibrous mass, as shown in Figure 3.10, consisting of filaments with a diameter of about 30 μm . X-ray diffraction of this fibrous material indicated that it was essentially copper with displaced diffraction lines as shown in Figure 3.11, suggesting lattice distortion by dissolved impurities, presumed to be selenium or possibly indium. The displacements of the peaks correspond to a lattice parameter increase of about 2 %. Sections cut through the last zone to freeze of the copper excess ingots also showed copper phase regions here. Examination of the four point resistivity and hot probe numbers in Table 3.3 indicates no significant change in apparent hole concentration with increase in copper content from one ingot to the next. However, surprisingly, at the end of each copper excess ingot, the resistivity adjacent to the precipitated copper areas was significantly *higher* than that at the middle of the ingot,

where copper areas were absent. When the distinct copper-precipitated areas at the ingot ends were encountered in the probe tests, the hot probe voltage was small at about +0.45 mV and the resistivity was too low to measure, consistent with the high electron concentration in the metal.

3.6 DISCUSSION

The Bridgman growth experiments with CuInSe_2 , confirm the important role of the selenium stoichiometry in the ternary compound, particularly for a deficiency of this element. In this case, it would seem that the progressive freezing in the Bridgman growth process takes place at first with near stoichiometric proportions but still with a sufficient selenium deficiency to make the material n-type; eventually with continued solidification, the selenium supply effectively runs out or is greatly diminished in the last zone to freeze, giving rise to the formation of the binary compounds. In the ingots prepared with excess copper, this element was precipitated at the last surface to freeze, even for the ingot with the lowest excess having the melt composition $\text{Cu}_{1.1}\text{InSe}_2$. The precipitation was in the form of 30 μm diameter filaments of copper with evidence of dissolved selenium or indium. The probe tests on the copper excess ingots showed no evidence of increased hole concentration, in the middle of the ingot, with increased copper content. Thus, these results are consistent with the ternary phase diagrams [3.8], indicating that the solubility of copper in CuInSe_2 is very small. More surprising is the observation of apparent *increased resistivity in the chalcopyrite in areas adjacent to precipitated copper regions* within the last zone to freeze, compared to material in the rest of the ingot, which was free of precipitated copper. Such a result would seem to imply that the CuInSe_2 may be more intrinsic in regions near the

precipitated copper than elsewhere. This will need to be checked in future work, along with further analysis of other nonstoichiometric preparations.

Table 3.1
CuInSe₂ Bridgman Growth Conditions

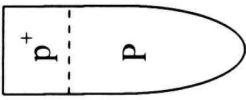
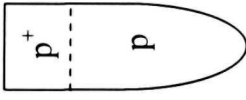
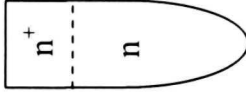
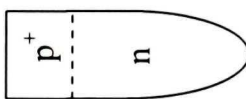
Run number	DH-B01	DH-B02	DH-B03	DH-B04	DH-B05	DH-B06	DH-B07
Cu:In:Se (weight, grm)	1.7:3:4.1	2.2:4:5.5	2.2:4:5.5	3.3:6:8.3	3.3:6:8.3	3.3:6:9.1	3.3:6:7.1
Cu:In:Se (molecular)	1:1:2	1:1:2	1:1:2	1:1:2	1:1:2	1:1:2.2	1:1:1.8
Number coatings with BN	2	2	2	1	1	2	1
Reaction time of In-Se (hr) ¹	1	1	9	24	10	33	24
Soak time at 1100°C (hr)	10	18	72	49	49	59	60
No. ampoule agitations	None	None	15	10	10	10	12
Ampoule lowering rate (mm/hr)	—	5.8	4.7	5.4	5.2	5.3	5.3
Cooling rate (°C/hr)	Natural cooling	29	15	15(700-650°C) 50(650-25°C)	20	20	20
Conductivity type	n&p	n&p	p	p	n&p	p	n
Lower furnace temp.	700°C	700°C	700°C	700°C	700°C	700°C	700°C
Comments	Ampoule dropped causing crack. Grainy appearance.	Ingot not uniform because of no agitation. Grainy appearance.	Good ingot. No sticking. Some faceting.	Good ingot. No sticking. Some faceting.	Crack in ampoule. Ingot sticking. Darker.	Ingot mostly p type. End p ⁺ type.	Ingot n type. End multi-phase.

Notes: ¹ Reaction temperature greater than 300 °C.

Table 3.1 (continued)
CuInSe₂ Bridgman Growth Conditions

Run number	DH-B08	DH-B09	DH-B10	DH-B11	DH-B12	DH-B13	DH-B14
Cu:In:Se (weight, grm)	4.3:6:8.3	4.3:6:8.3	4:6:8.3	4:6:8.3	3.7:6:8.3	3.3:6:8.3	3.3:6:8.3
Cu:In:Se (molecular)	1.3:1:2	1.3:1:2	1.2:1:2	1.2:1:2	1.1:1:2	1:1:2	1:1:2
Number coatings with BN	1	2	2	2	2	1	2
Reaction time of In-Se (hr)	34	44	24	36	28.5	24	24
Soak time at 1100°C (hr)	31.5	46.5	44	40	34	64	108
No. ampoule agitations	15	15	15	15	15	15	15
Ampoule lowering rate (mm/hr)	4.9	5.3	5.3	5.2	5.2	5.1	5.2
Cooling rate (°C/hr)	29	30	18	22	30	30	30
Conductivity type	p	p	p	p	p	n&p	n&p
Lower furnace temp.	700°C	700°C	650°C	650°C	650°C	650°C	650°C
Comments	Copper fibres on the last surface to freeze.	Copper fibres on the last surface to freeze.	Copper fibres on the last surface to freeze.	Copper fibres on the last surface to freeze.	Copper fibres on the last surface to freeze.	Ingot n type, end multi-phase, probably deficient in Se.	Ingot n type, end multi-phase, probably deficient in Se.

Table 3.2
Ingots prepared with selenium nonstoichiometry

Melt composition		CuInSe _{2.2}	CuInSe ₂	CuInSe _{1.8}	CuInSe ₂
Ingot number		6	3, 4	7	5
Electrical resistivity ¹ (Ωcm)	middle	6.4	7.3	1.4	14
	end	0.24	1.8	0.21	4.8
Hot probe voltage ² (mV)	middle	-37	-26	+36	+11
	end	-3.6	-2.9	+5.3	-4.5
Conductivity type					

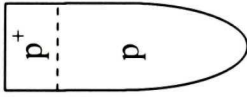
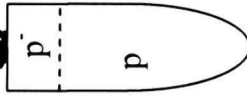
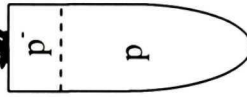

Notes:

¹ Four point probe readings.

² Hot point heater voltage set at 30 V.

Table 3.3

Ingots prepared with excess copper

Melt composition	CuInSe ₂	Cu _{1.1} InSe ₂	Cu _{1.2} InSe ₂	Cu _{1.3} InSe ₂
Ingot number	3, 4	12	10, 11	8, 9
Observed Cu at end	none	fibres	fibres	fibres
Electrical resistivity ¹ (Ωcm)	middle end	53 350 (0) ³	21 190 (0) ³	14 105 (0) ³
Hot probe voltage ² (mV)	middle end	-26 -2.9	-3.6 -10 (+0.45) ³	-8.5 -7 (+0.51) ³
Conductivity type				

Notes:

¹ Four point probe readings.

² Hot point heater voltage set at 30 V.

³ Readings on precipitated copper area on ingot end surface.

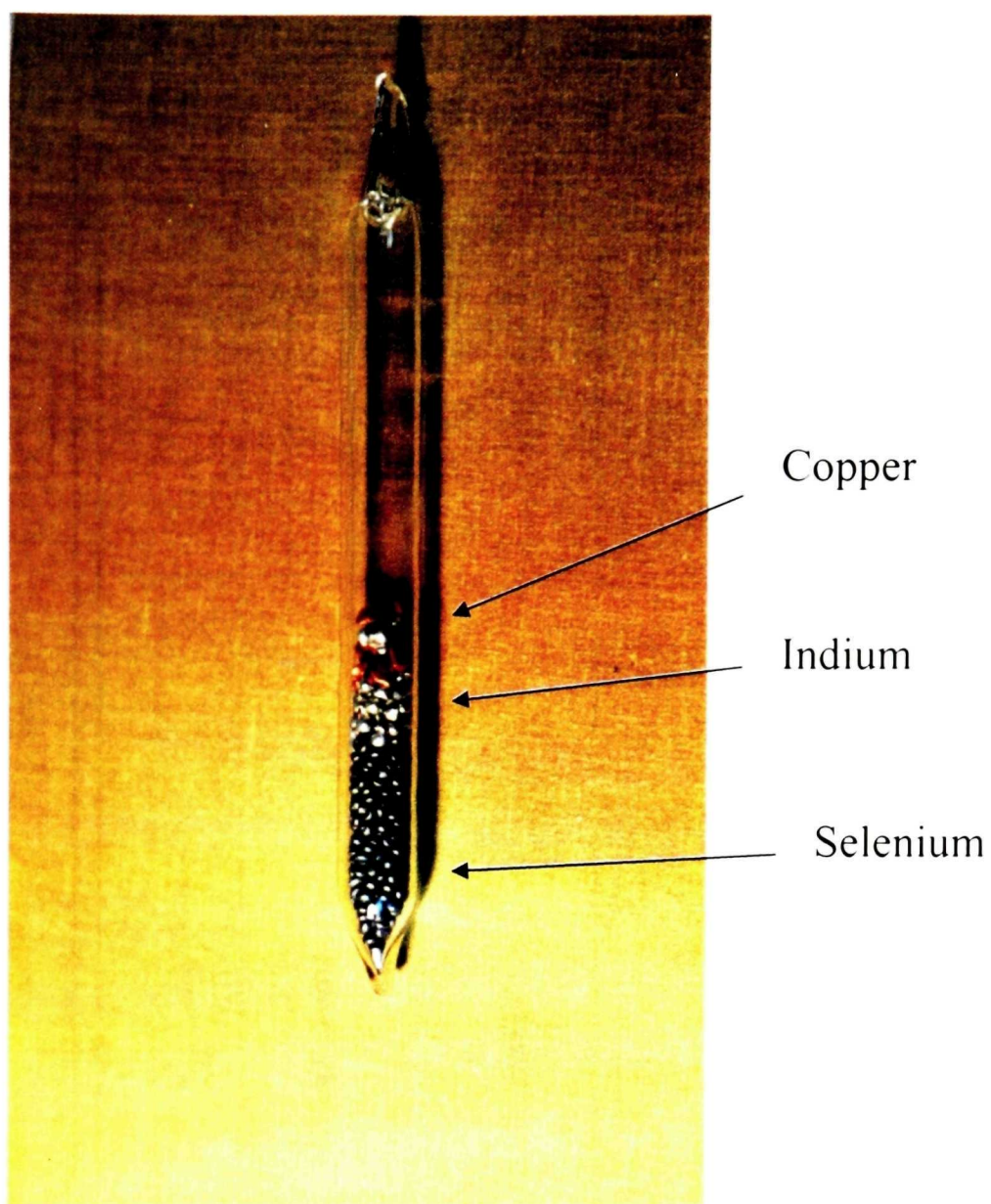


Figure 3.1 Photograph of a sealed quartz ampoule with charged pellets.

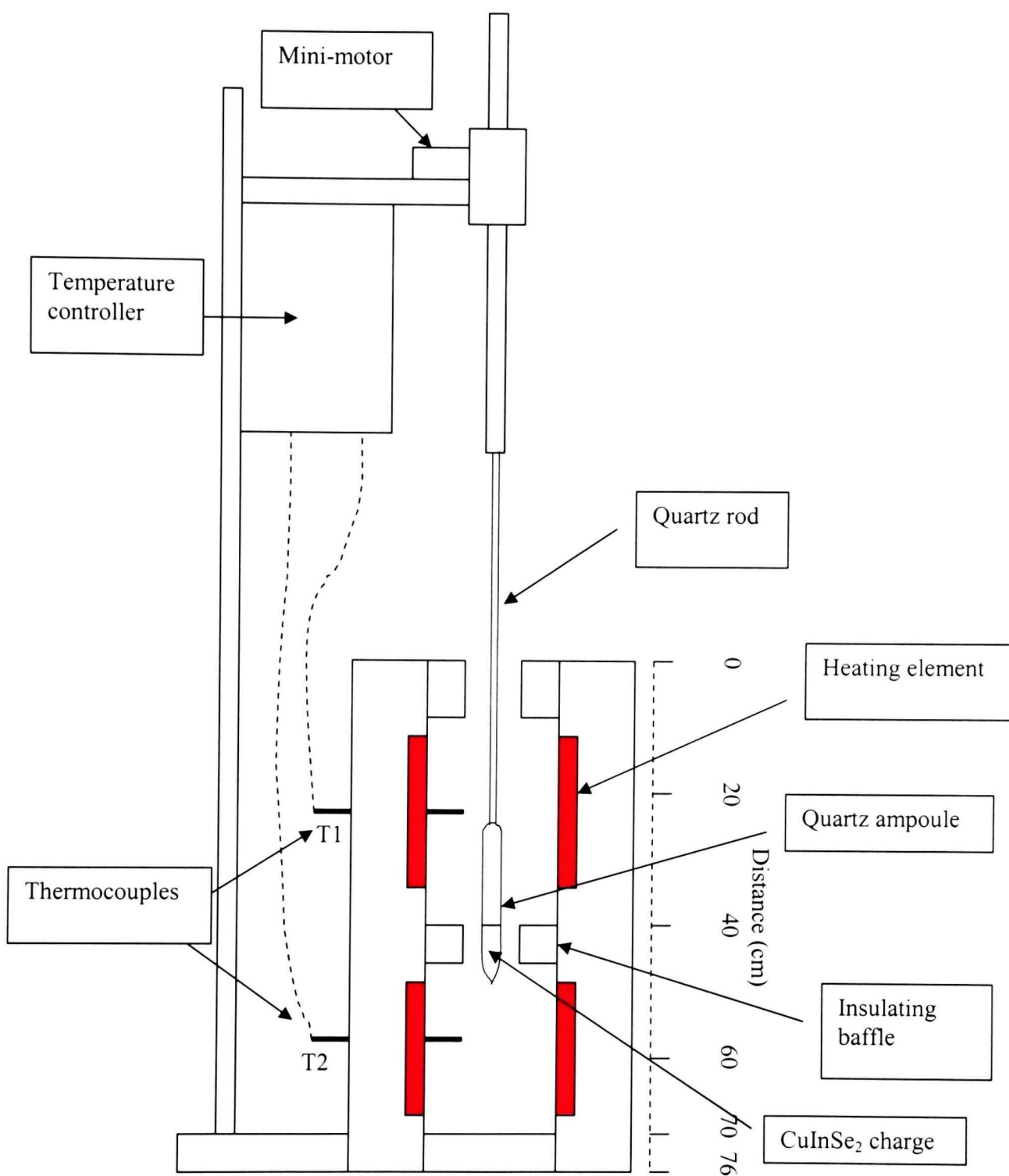


Figure 3.2 Schematic of vertical Bridgman furnace and ampoule lowering system.

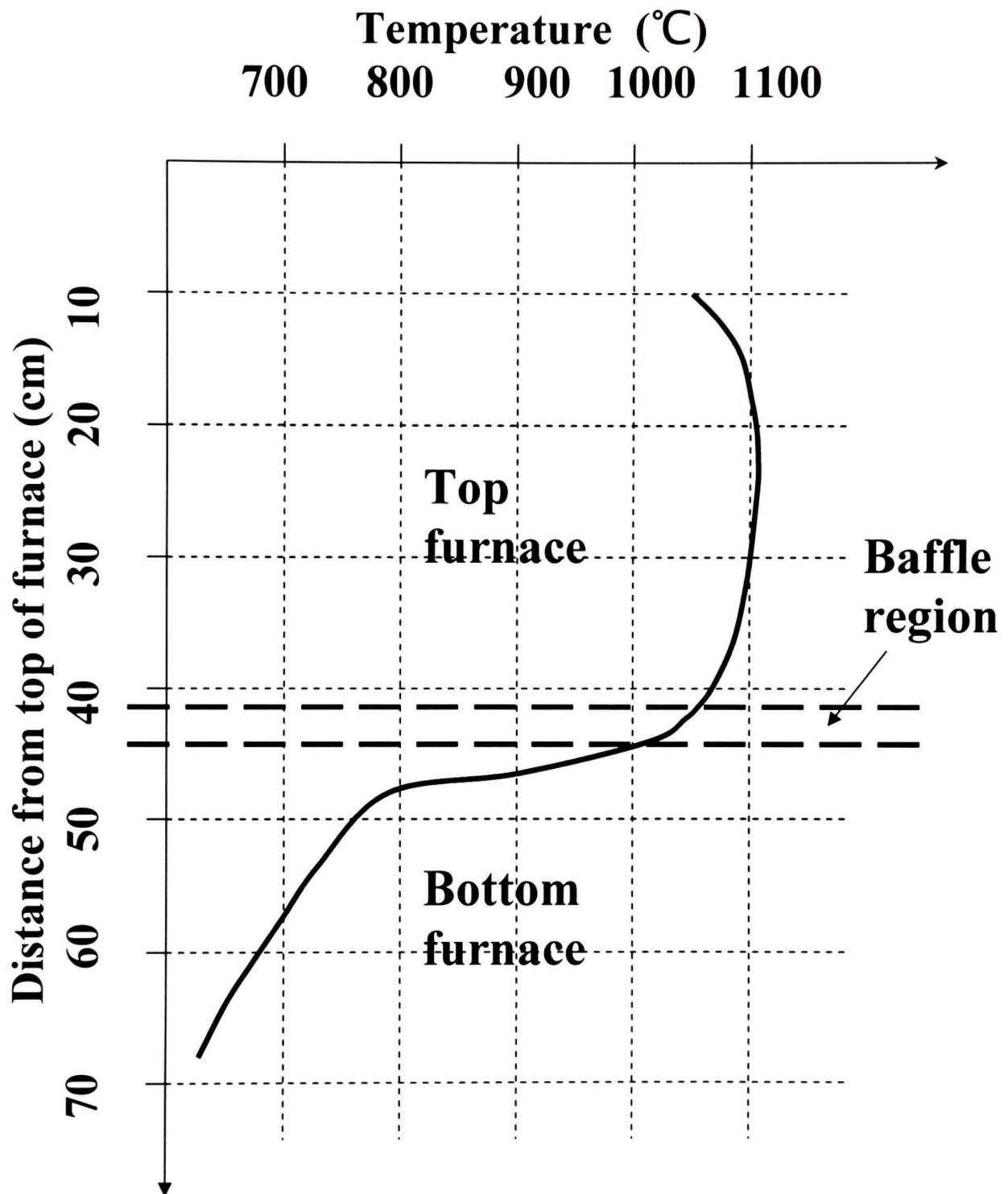


Figure 3.3 Temperature profile in the vertical Bridgman system.

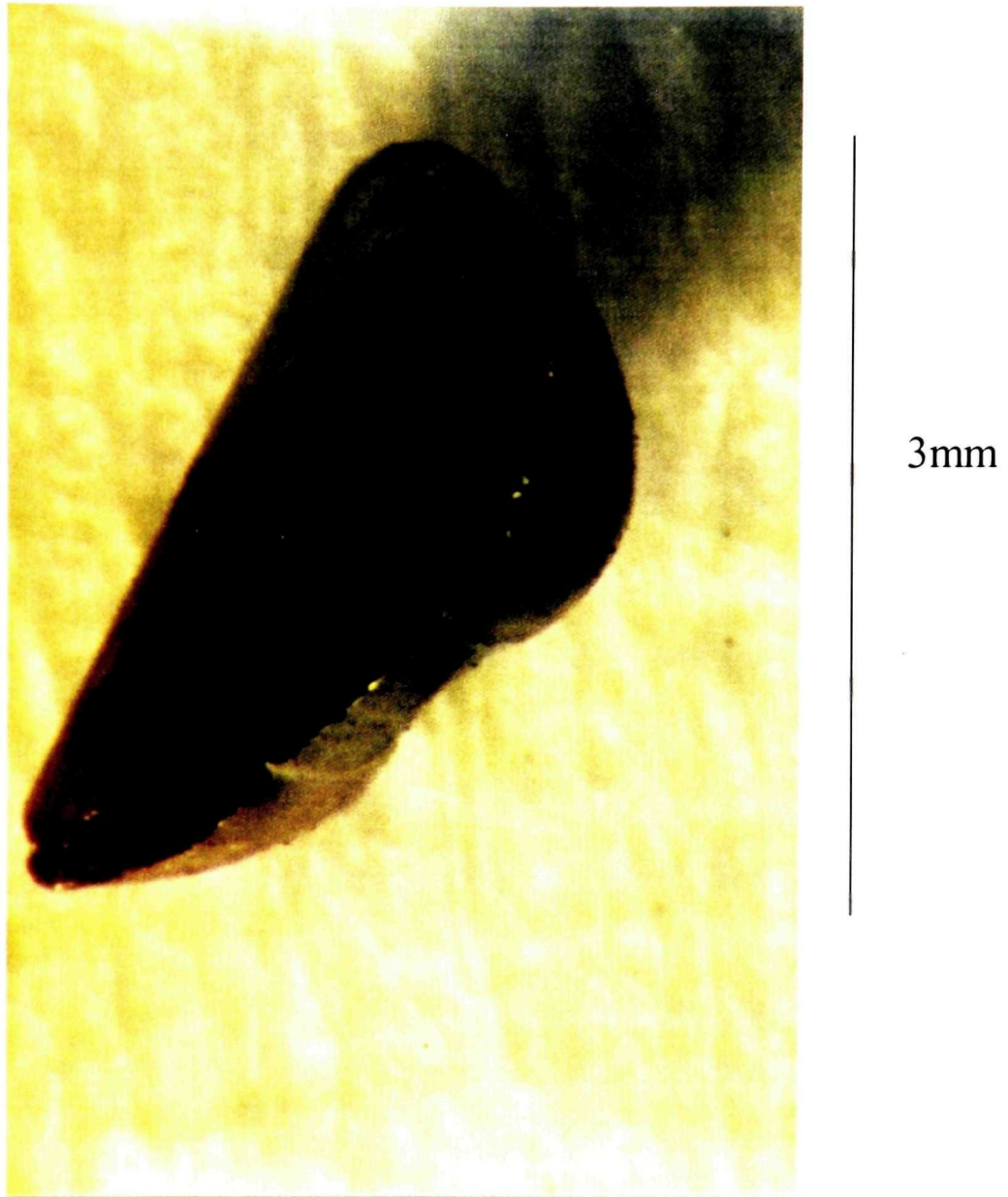


Figure 3.4 Photograph showing a cleavage face in a piece from ingot DH-B06.



1.5cm

Figure 3.5 Clear twin-lines in a piece from ingot DH-B04.

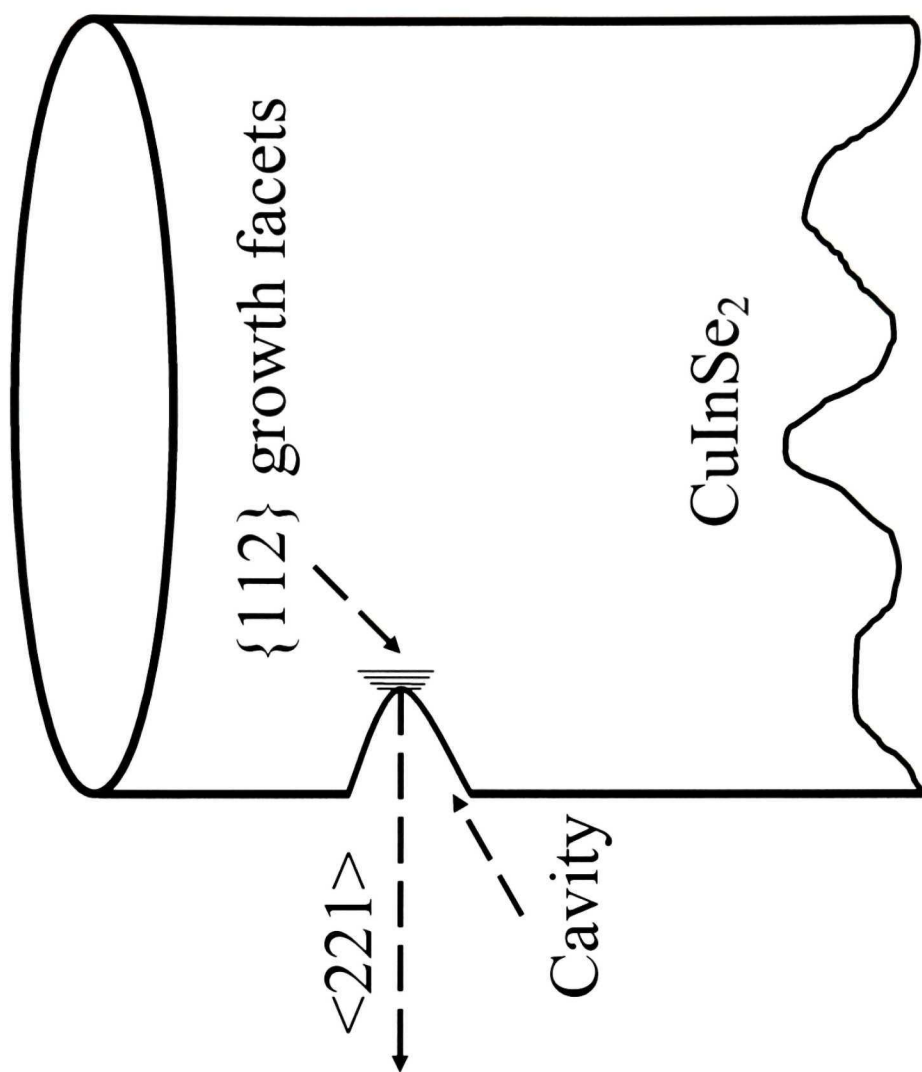
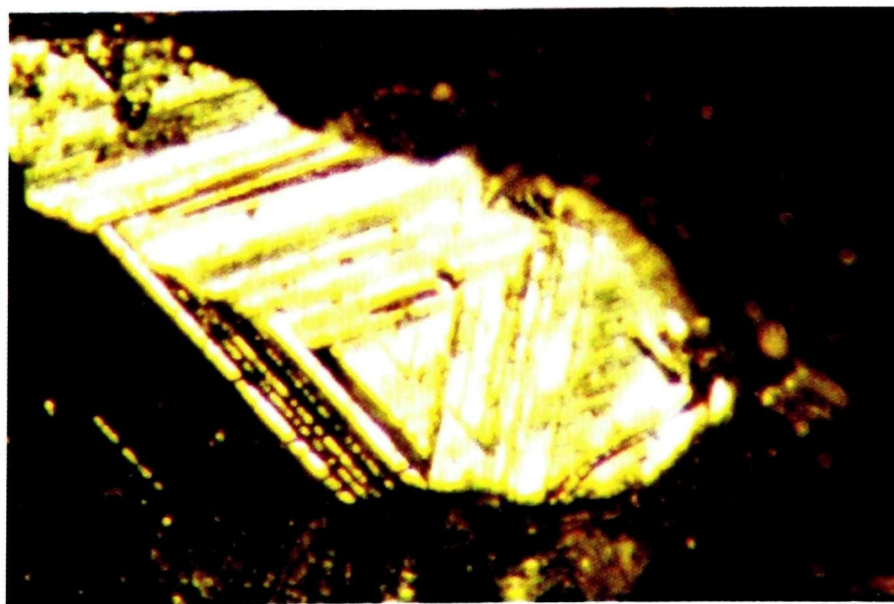


Figure 3.6 Triangular growth facets, in a $\{112\}$ plane, as seen at the bottom of a side cavity in stoichiometric CuInSe_2 Bridgman-grown ingot DH-B13.

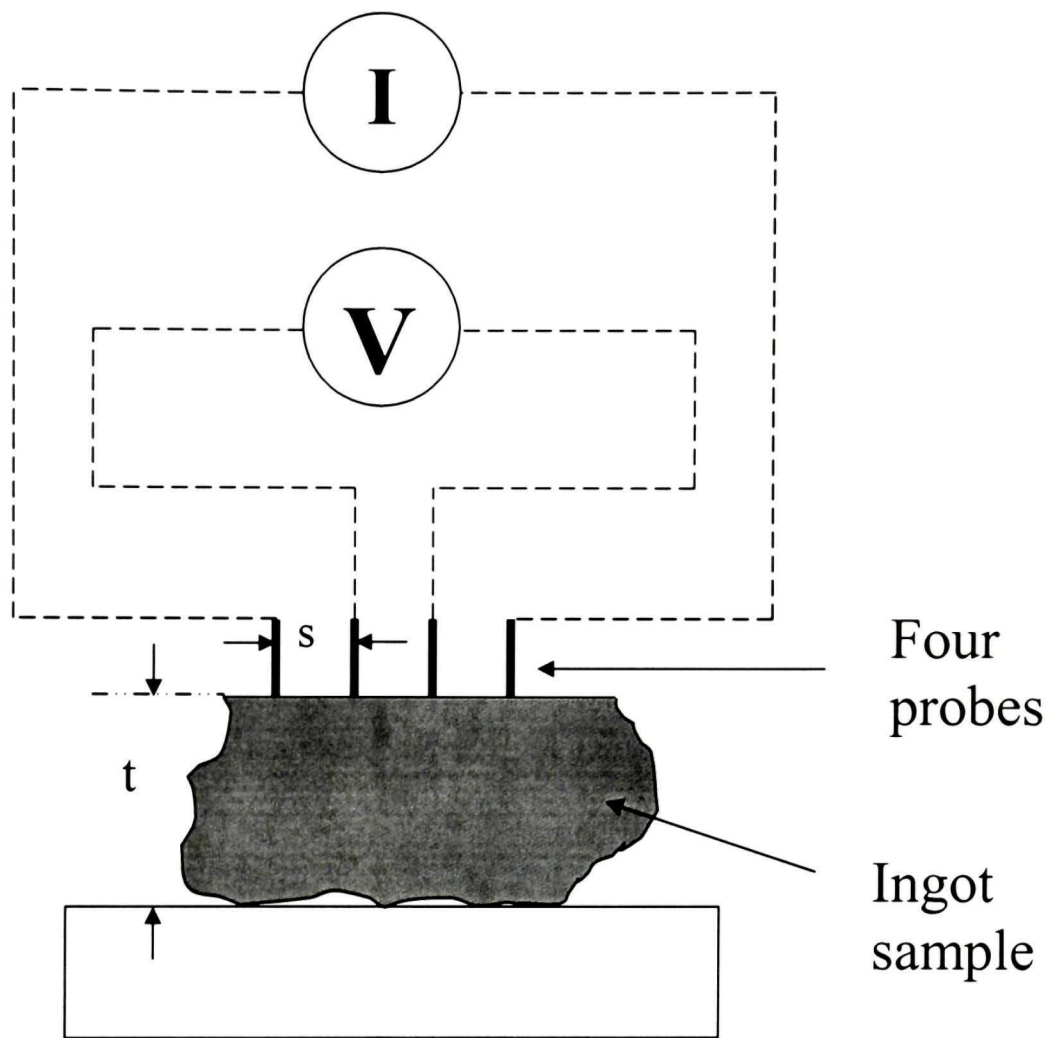


Figure 3.7 Schematic of four-point probe for resistivity estimation.

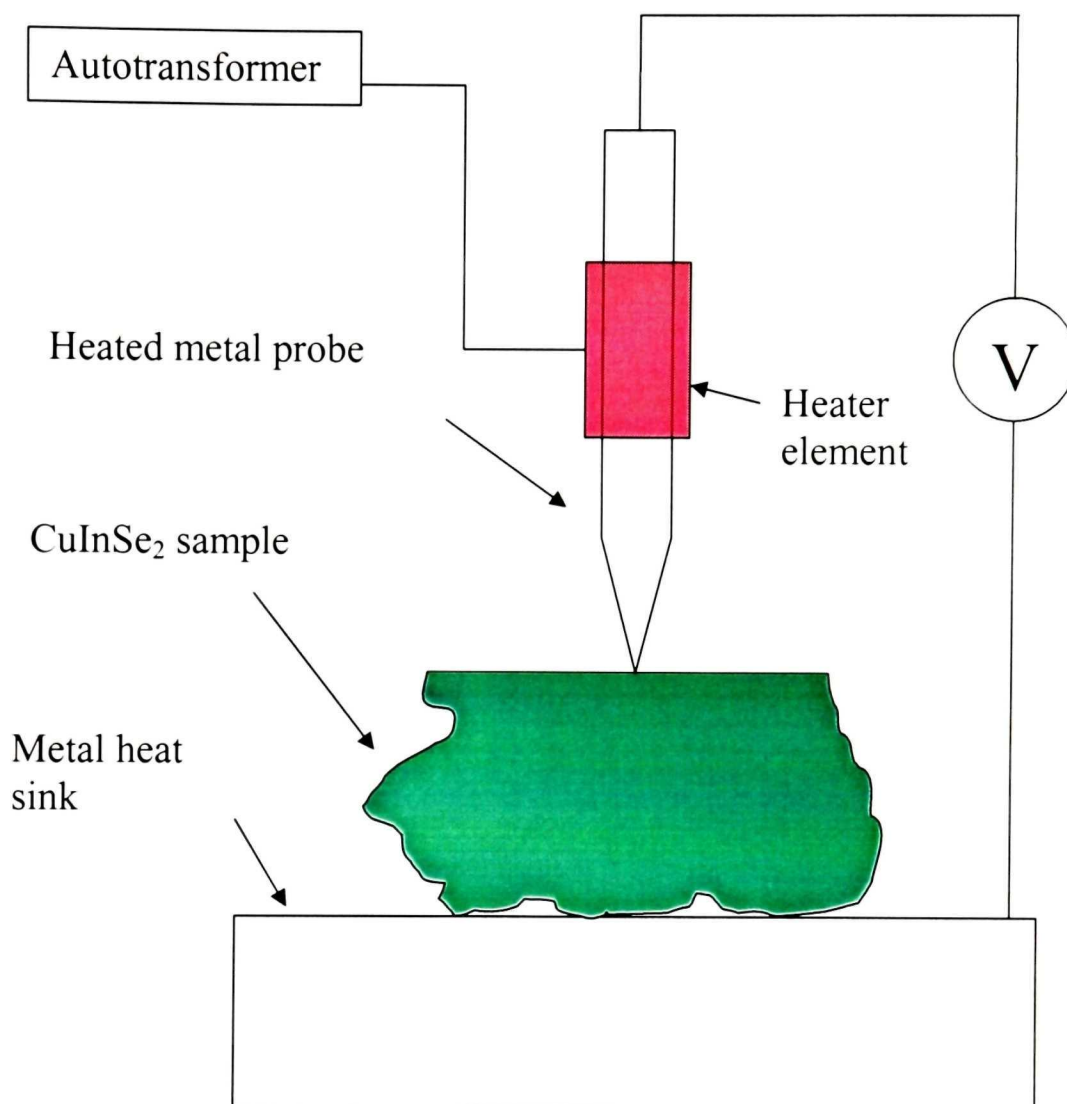


Figure 3.8 Schematic of the hot probe setup used for conductivity type determination.

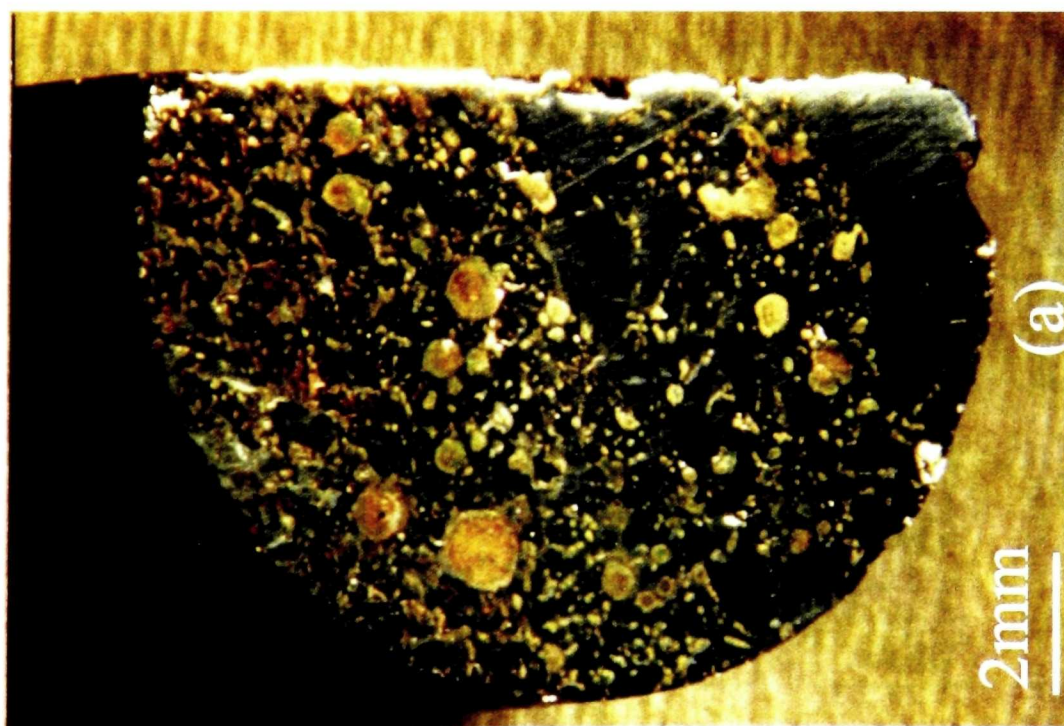


Figure 3.9 Surface of two slices cut across ingot DH-B07, prepared with a selenium deficiency, corresponding to a melt composition of $\text{CuInSe}_{1.8}$; (a) from last end to freeze after etching, (b) from middle of ingot.



Figure 3.10. Copper fibres with a diameter of about $30\text{ }\mu\text{m}$, precipitated at the last surface to freeze of the excess copper ingot DH-B10.

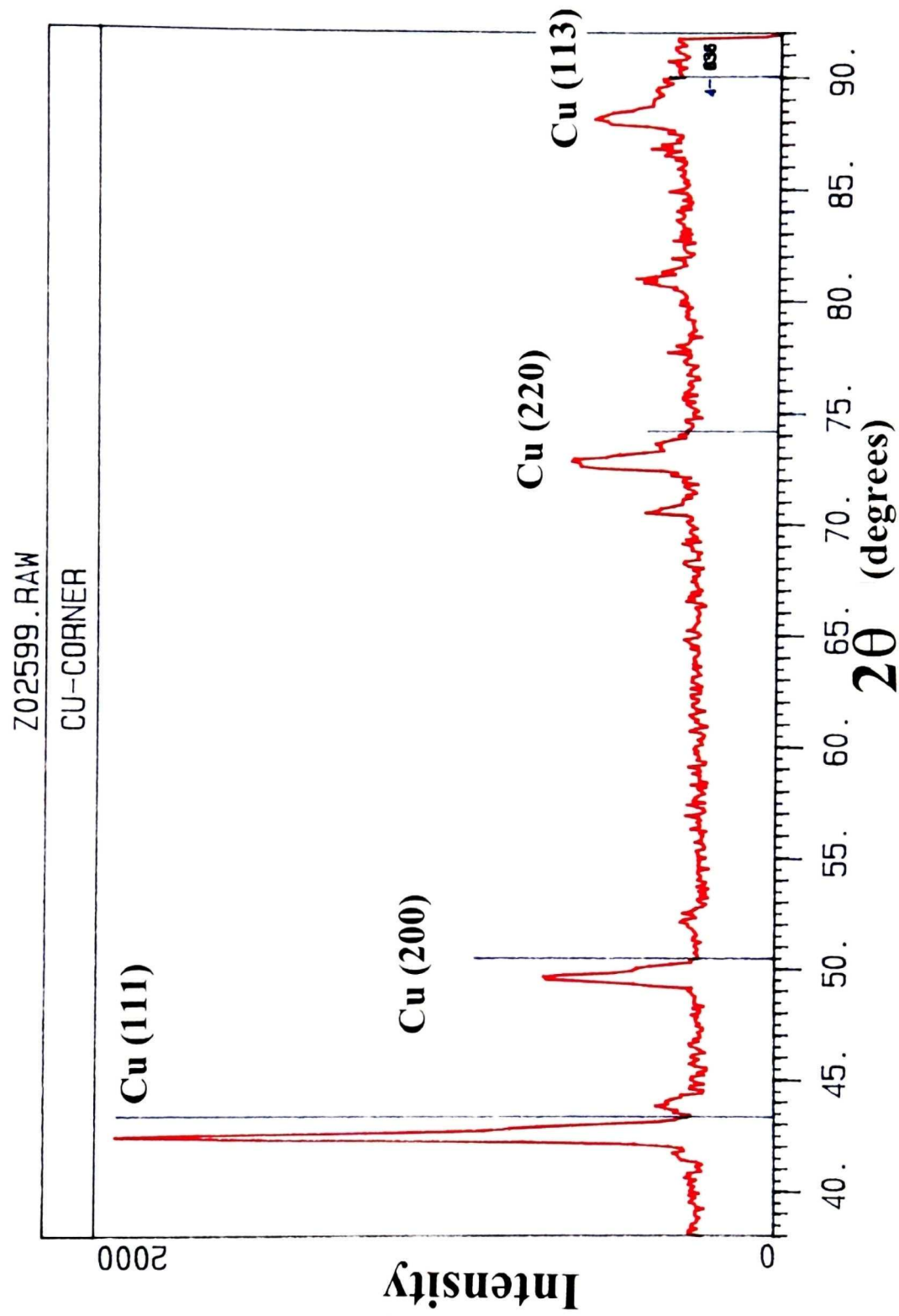


Figure 3.11 X-ray diffraction pattern of the copper fibres shown in Figure 3.10, together with 4 diffraction lines for pure copper.

Chapter 4

Fabrication of Photovoltaic Cells

4.1 INTRODUCTION

A number of photovoltaic cells were prepared from the Bridgman-grown ingots with the fabrication process described in detail in this chapter. However, first a brief outline may be helpful. The layer structure of each device was Au-CuInSe₂-CdS-ZnO-In, as shown schematically in Figure 1.1.

A slice was first cut from an ingot and lapped on both faces. One surface was then fine-polished and etched. Then the wafer was annealed in argon, following which it was coated with a thin film of CdS by immersion in a chemical bath. Next, gold was evaporated on the back lapped face. After this, a layer of doped ZnO was deposited, via a metal mask, by rf sputtering on the CdS and two stripes of indium were evaporated on the ZnO area to act as the illuminated side electrical contacts. Finally, fine copper wires were soldered to these contacts and electrical contact to the gold backing of the wafer was made to yield a completed photovoltaic cell. The procedures used mostly followed those employed by Shukri [1.11], Yip [1.4] and Al-Quraini [4.1], formerly of this laboratory. In particular, the annealing step, prior to film deposition, consisting of heating the wafer in argon at 350°C for 2 hours, was found by Yip [1.4] to be necessary for obtaining good cell photovoltaic performance.

4.2 CuInSe₂ WAFER PREPARATION

4.2(a) Wafer Polishing

Starting with a p-type Bridgman-grown ingot, a slice was cut from it using a diamond-bonded cutter wheel with a wafer thickness of 1 to 3 mm. While a smaller thickness would be desirable from a device point of view, the material is brittle and can break easily. The wafer was then cleaned in trichloroethylene (TCE) and acetone (ACE) and given a rinse in de-ionized (DI) water. It was next tested with a hot probe to confirm its p-type conductivity. With the heater voltage of the hot probe set to 30 volt, the thermoelectric signal was usually about -35 mV uniformly across the wafer. After this, the wafer was attached to a metal holding block with wax and each face was lapped on a rotating wheel using 600C-grit Leco silicon carbide paper. Next, one of the two surfaces was given a fine polishing treatment, which consisted of first polishing with a 6 μm Leco Aerosol diamond spray and kerosene oil for 30 minutes, then with a 1 μm spray and kerosene oil for another 30 minutes and finally a polish using 0.05 μm alumina paste with DI water for yet another 30 minutes. After polishing, the wafer was detached from the handling block and the surplus wax on it was removed with several applications of TCE for more than 2 hours. Following this, the wafer was immersed in acetone for 5 minutes to remove the TCE and then thoroughly rinsed with DI water. The resulting polished face was free of scratches visible to the eye but finer ones were observable under an optical microscope.

4.2(b) Wafer Etching

After polishing, the wafer was etched in a solution of methanol with 0.5% by volume of bromine added for a period of less than 1 minute. This was followed by a wash

in DI water. The purpose of the etching was to improve the surface for the subsequent deposited layers.

4.2(c) Wafer Annealing

In the wafer annealing step, the procedure was as follows. The wafer was inserted within the glass tube of a horizontal furnace (Figure 4.1), with argon gas flow controlled by a flux controller. To minimize possible contamination from the glass, the polished face of the wafer was arranged to be uppermost within the tube. Since Yip [1.4] reported that oxygen had a deleterious effect on the cells, the tube was flushed through with argon gas for 30 minutes before raising the temperature. After this, the temperature was raised to 350°C, as indicated by a thermocouple, and maintained at this value for 2 hours. At the end of this period, the furnace power was turned off and the tube allowed to cooling with a continuous flow of argon. The wafer was retrieved from the furnace only after cooling to room temperature.

4.3 LAYER DEPOSITIONS

4.3(a) CdS Deposition

A thin film of CdS was next deposited on the polished face of each wafer in the following way. First two aqueous solutions, A and B were prepared. Solution A was a mixture of CdCl₂ (cadmium chloride), NH₄Cl (ammonium chloride) and (NH₂)₂CS (thiourea) in the molecular (M) proportions 2 mM: 20 mM: 20 mM respectively, while solution B was a 200 mM NH₄OH (ammonium hydroxide) solution. The arrangement shown schematically in Figure 4.2 was used in the treatment, where a larger beaker of water, containing a smaller beaker, was heated on a hotplate. First 25mL of solution A

was introduced into the smaller beaker and an equal quantity of solution B was added to it and mixed with a glass rod at room temperature. The resulting solution should have a pH of 11, as monitored with pH test paper. With the water in the larger beaker already heated to 70°C from the hotplate, the smaller beaker was placed within the water. After about a minute, the wafer, supported on a molybdenum holder, was lowered into the heated solution in the smaller beaker and maintained immersed for 8 minutes, after which it was removed and given a rinse in DI water. Under these conditions, it has been reported that the thin coating of CdS deposited has a thickness of 30-50 nm and an electrical resistivity of about 10^5 ohm cm.

4.3(b) Gold Back Contact

Following the CdS deposition, gold was evaporated on the lapped face of the wafer. This was done in a conventional vacuum coating system using gold wire of diameter 0.25 mm and length 15 cm, as the source in a molybdenum boat.

4.3(c) ZnO Deposition

A single layer of low resistivity ZnO was next deposited on the CdS by rf magnetron sputtering. The sputtering system for doing this is shown schematically in Figure 4.3 and includes a Varian turbo pump, a four inch U.S. Inc. sputtering gun and an Advanced Energy Co. rf power generator. The target consisted of a ceramic disc of ZnO containing 2% of Al_2O_3 to reduce the resistivity of the deposited layer. As indicated in Figure 4.3, several samples could be sputtered at the same time, where each of these was positioned at an angle of 45° to the plane of the target and located about 4 ½ cm above it. The angular positions reduce direct ion bombardment to the sample and result in

improved film quality. In the present case, the wafer was located in the system with a metal mask in front of it to limit the ZnO area deposited - usually in the form of a circle. The wafer was often accompanied, in the sputtering system, by a glass microscope slide for monitoring the film thickness and resistivity. At the beginning, the chamber was pumped down to a vacuum pressure of 10^{-6} torr to remove as much air as possible. The argon gas was allowed to flow through the system reaching a chamber pressure of about 200 millitorr. After pressure stabilization, the rf power was switched on and the power was maintained at 80 watts. When the plasma was formed, the argon gas flow was reduced until the pressure reached 60 millitorr, at which value it was maintained for the duration of the sputtering period of some 8 hours. This produced a ZnO film on the CdS with a thickness of about $0.7 \mu\text{m}$ and a sheet resistance of $100\Omega/\square$, corresponding to a bulk resistivity (ρ) of $7 \times 10^{-3} \Omega\text{cm}$. A two layer ZnO deposition, one without Al_2O_3 inclusion, as employed in polycrystalline thin film cells [4.2], was tried but not found to be better than a single doped layer.

4.4 FURTHER STEPS

4.4(a) ZnO Thickness and Resistivity

The above mentioned values of film thickness (d) and sheet resistance (ρ/d) were obtained from measurements on the ZnO layer deposited on the glass slide, sputtered at the same time as the wafer itself. The thickness was obtained by counting the number of coloured interference fringes (N) near the film edge and noting the ZnO area central colour and its corresponding wavelength λ . Then, the thickness was obtained using the

formula: $2nd = (N - 0.5)\lambda$, where n is the refractive index of ZnO, taken as 2.0, and the value in the bracket of 0.5 arises from the phase change of the reflection at the film surface. Thus, usually $N = 6$ for an 8 hour sputtering operation and taking $\lambda = 0.5 \mu\text{m}$ (for a green central colour), the calculated film thickness would be $d = (6-0.5) \times 0.5 / (2 \times 2) = 0.69 \mu\text{m}$.

The film electrical resistivity was obtained using the four point probe (Figure 3.7) on the film. Here, the formula for a sheet of infinite area was employed namely: $\rho = 4.53Vd/I$ [3.4], where I is the current through the two outer probes and V is the voltage between the two inner probes. Then the sheet resistance is just $\rho/d = 4.53V/I$.

4.4(b) Contact Stripes and Cell Mounting

Following the sputtering, two stripes of indium were deposited on the ZnO area in a vacuum coater by evaporation through a metal mask. The dimensions of the two mask openings were $2 \times 0.2 \text{ mm}$. Then the wafer, with its gold coated face adjacent to the flat end of a cylindrical aluminum stud, was attached to it, using silver paste and the stud itself was inserted into a circular plastic holder (Figure 4.4) containing brass screws to act as terminal posts. Next, very fine copper wires were soldered to the two indium stripes using low melting point (71°C) Wood's metal. The other ends of these wires were soldered to the brass terminal posts with regular electronic solder to act as the electrical contacts to the ZnO. Electrical contact to the gold backing of the wafer was made via a metal screw to the aluminum stud. With this done, the cell was completed and ready for testing. A photograph of the ZnO area of the device is shown in Figure 4.5.

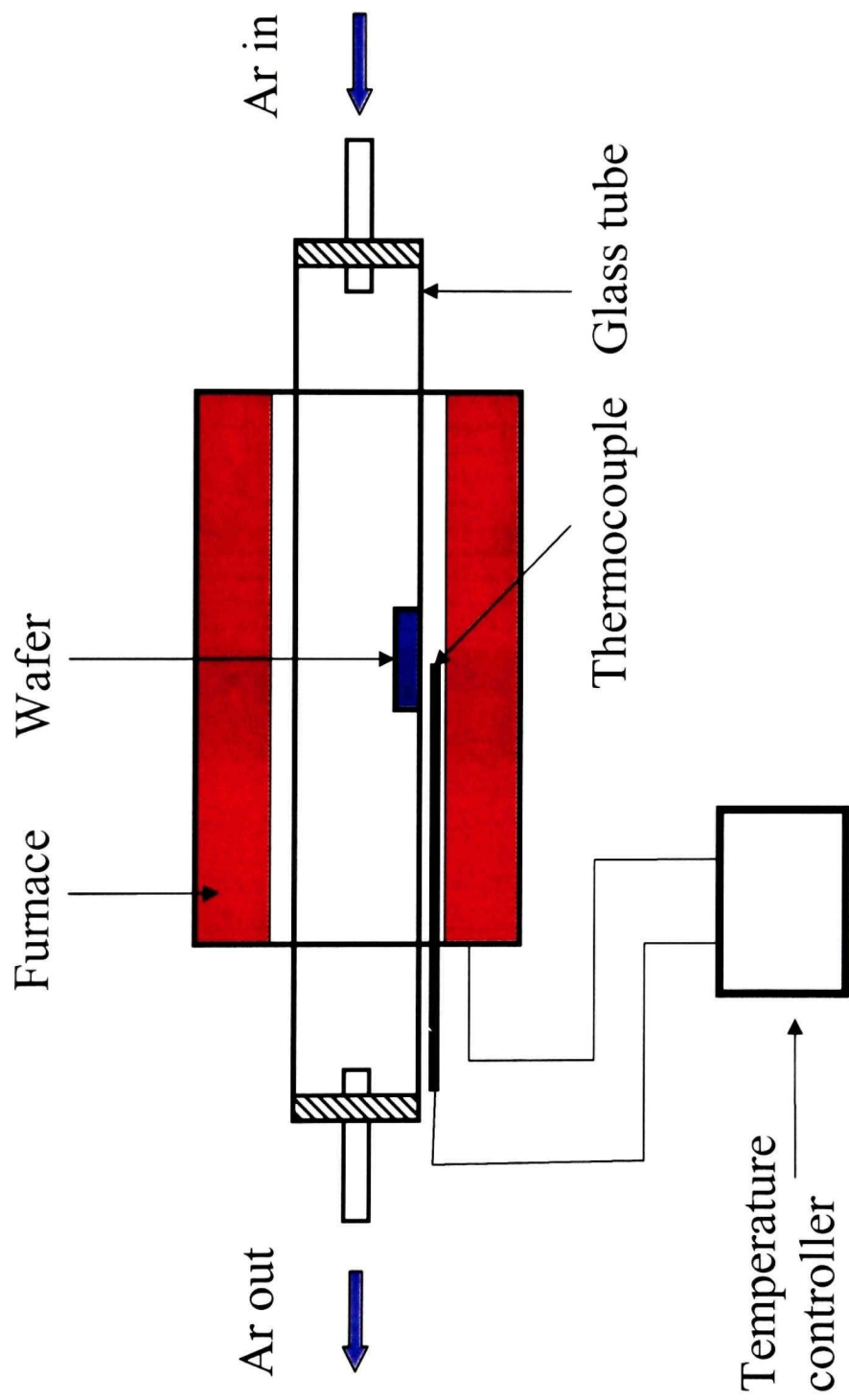


Figure 4.1 Schematic of furnace for the annealing step of the CuInSe_2 wafer.

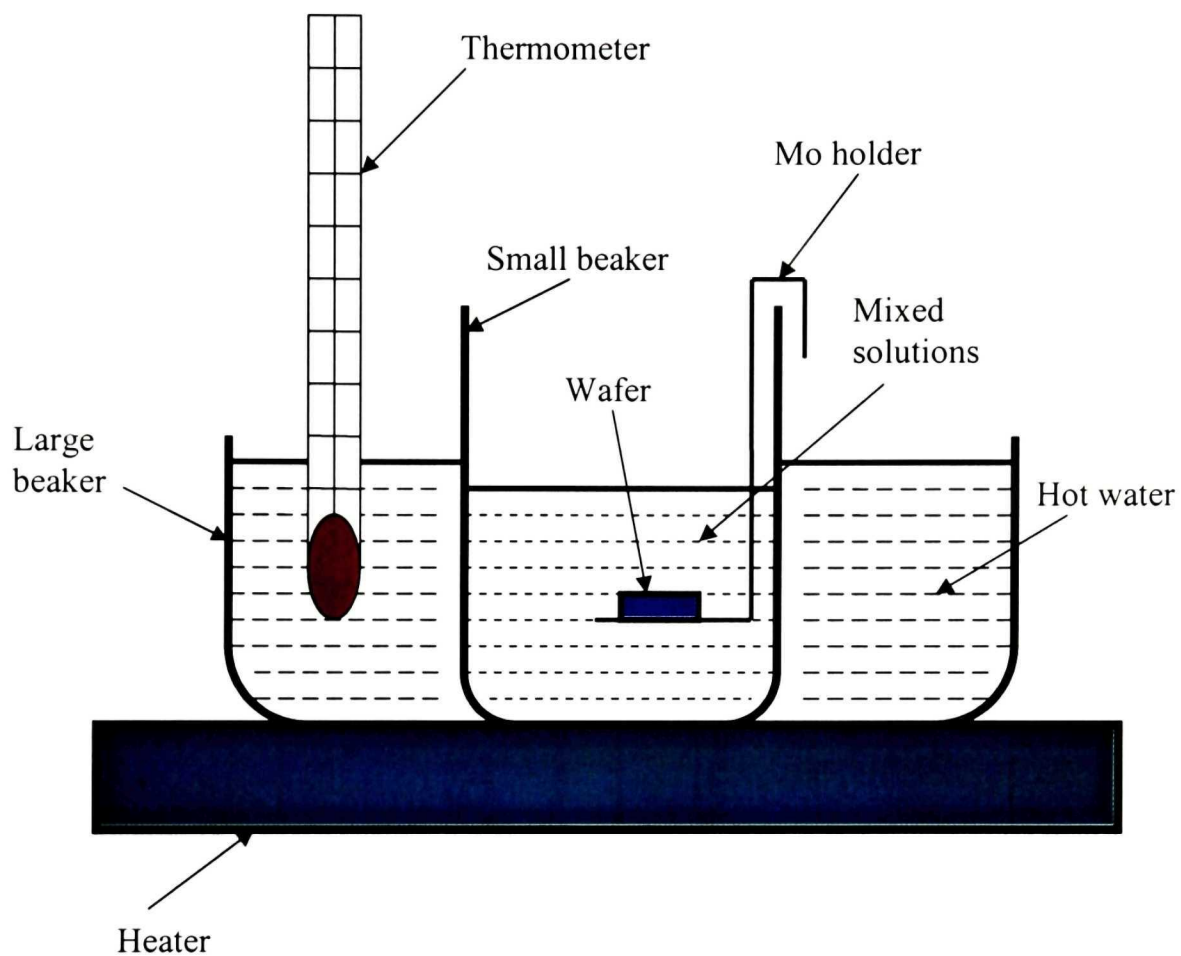


Figure 4.2 Schematic of set up for depositing CdS film by a chemical bath method.

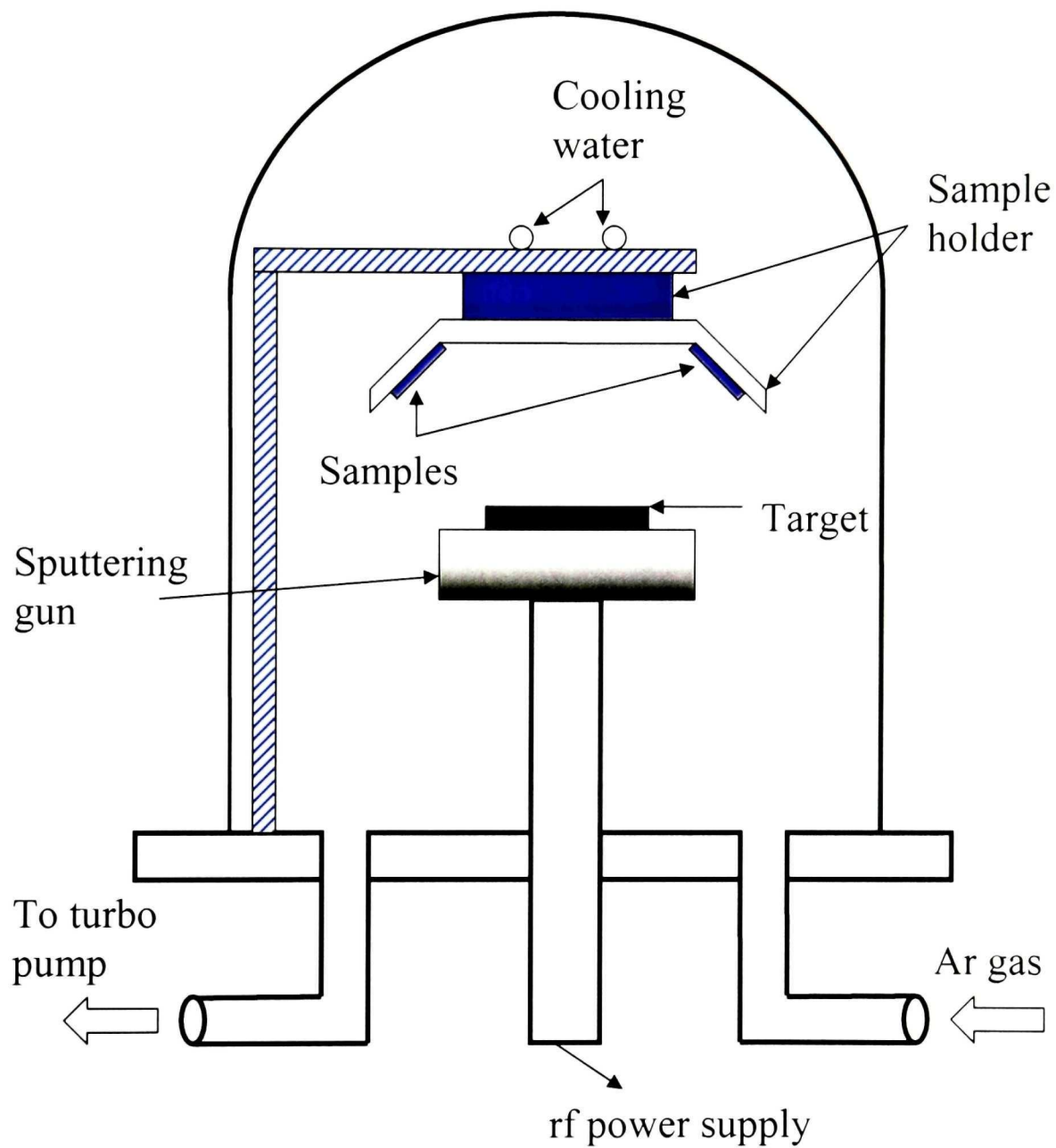


Figure 4.3 Schematic of the rf sputtering system for the ZnO layer deposition.

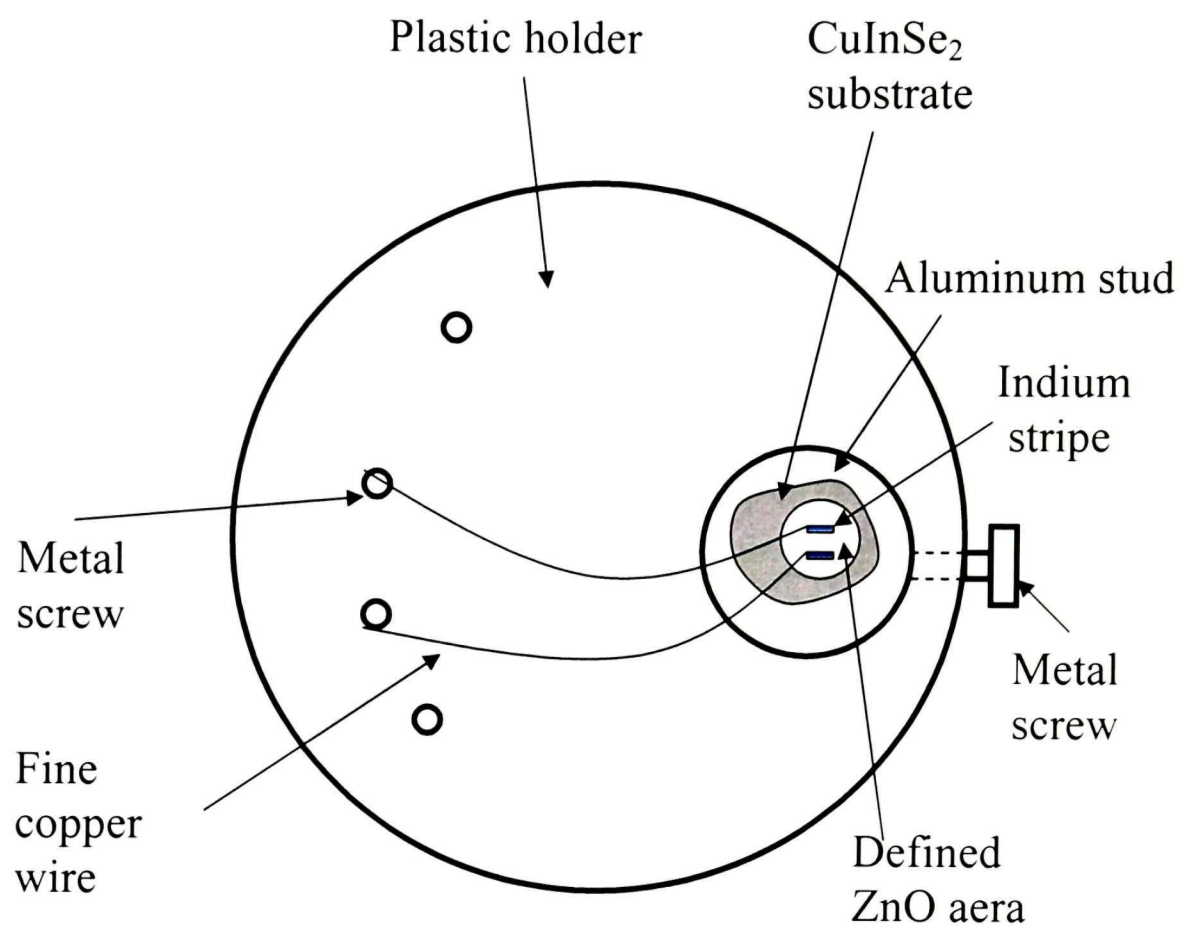


Figure 4.4 Schematic of the mounting arrangement of the fabricated cell in a plastic holder.

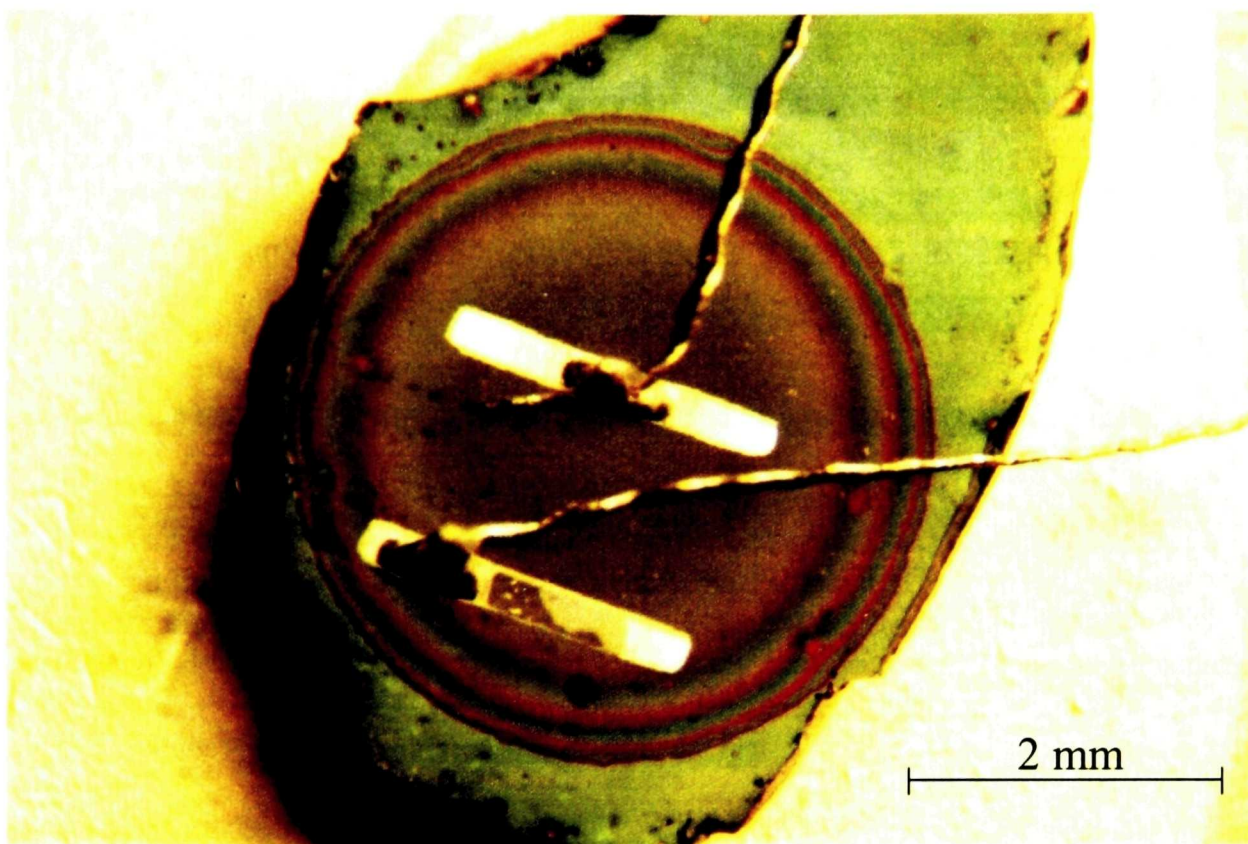


Figure 4.5 Photograph of cell DU-35, showing the circular ZnO area and the two indium contact stripes.

Chapter 5

Cell Characteristics Under Illumination

5.1 INTRODUCTION

In developing the fabrication processes, described in chapter 4, for the Au-CuInSe₂-CdS-ZnO-In cells, many devices were made. While all were given preliminary performance tests, only those developed later in the program were examined more closely and, of these, only 5 cells were subjected to more detailed measurements, which are reported in this chapter, with particulars included in Table 5.1. These measurements were current-voltage characteristics under illumination and darkness and photoresponse characteristics from about 400 to 1,400 nm wavelength. The first two sections of the chapter present these results for all 5 cells. Capacitance measurements were also carried out. They are described in chapter 6.

It will be seen that among the 5 devices, cell number DU-35 showed the best photovoltaic performance and hence results on this device are specially presented in the third section (5.4). To check the validity of the results on this cell, it was submitted to the National Renewable Energy Laboratory (NREL) in Golden, Colorado for tests and a comparison of results is also presented here.

5.2 CURRENT-VOLTAGE MEASUREMENTS

5.2(a) Under Sunlight

Measurements of current-voltage (I-V) characteristics on all 5 cells were made under direct sunlight with cloudless conditions at noon in Montreal (latitude $45^{\circ} 31'$) on different days. Figure 5.1 shows a plot of current density j (current I divided by effective cell area) against voltage, measured on May 10th 2003. The current through the cell and voltage across it, were varied by changing the value of a variable resistor, as shown schematically in Figure 5.2. Using an Eppley model PSP pyranometer, the solar irradiance was monitored to be about 100 mW/cm^2 . From the maximum power point of each curve, the conversion efficiency (η) was calculated and the values for each cell are listed in Table 5.1, along with values of open circuit voltage (V_{oc}), short circuit current density (j_{sc}) and fill factor (F.F.). It is noted that the two best cells, DU-22-1 and DU-35, had apparent efficiencies of 8.1 and 9.4 % respectively and an open circuit voltage of 0.48 volt on the day of the exposure.

5.2(b) Simulated Sunlight

Measurements under simulated sunlight were made on the cells using a xenon arc lamp with an optical filter. In a diverging light beam, the irradiance at the position of the cell was adjusted to be 100 mW/cm^2 using a Solarex calibrated test cell. However, due to factors such as light pattern nonuniformity and lamp intensity variations with time, it is believed there could be an error of some $\pm 15 \%$ in the irradiance level. Nevertheless, readings under the simulator are useful, not only to take measurements when the sun is not available but also because more convenient measuring equipment within a laboratory can be used. In this case, the readings were taken with the circuit in Figure 5.3, where a voltage was applied to the cell, so that voltages in the reverse direction and in the forward voltage

direction beyond V_{oc} could be obtained. The current density-voltage plots for the 5 cells are shown in Figure 5.4 and comparison with the direct sunlight curves of Figure 5.1 indicates general agreement. The reciprocals of the slopes of the curves beyond V_{oc} generally reflect the illuminated series resistances of the cells and values of these are listed in Table 5.1, evaluated at about 0.5 volt. Here, it is noted that the two best cells, DU-22-1 and 35, had the lowest values of apparent illuminated area series resistance.

5.2(c) Dark Characteristics

The results of current density-voltage measurements, taken under darkness, are shown in Figure 5.5 on linear scales, where the different values of dark series resistance are reflected in the different inverse slopes above about 0.5 volt in the forward direction. Figure 5.6 shows the same data plotted on semilogarithmic scales.

Assuming a relationship of the form:

$$j = j_o [\exp(\frac{qV}{nkT}) - 1] \quad ,$$

the plots yield ideality n-factors of 2.1 to 2.7. Extrapolation to the j-axis, from the linear regions, yields values of the pre-factor current density j_o of 10^{-5} to 10^{-6} mA/cm². The curvature of the plots at higher forward j-values is due to cell series resistance.

5.3 PHOTORESONSE

Photoresponse measurements were made on all 5 cells over the wavelength range of about 400 to 1,400 nm using a Beckman Instruments model 2400 monochromator with a slit width of 1mm. The monochromator irradiance at the cell position was determined, at

each wavelength, with a calibrated silicon cell for the visible to near infrared range and with a calibrated InGaAs cell for longer wavelengths. Quantum efficiency (QE) values at each wavelength λ were obtained by multiplying the photoresponse in amp/watt by $hc/(q\lambda)$ and these QE values are plotted against wavelength in Figure 5.7. It is noted that all the values are below 80 %, indicating considerable light losses due to the absence of anti-reflection coatings on the cells.

5.4 CELL DU-35

Because of its superior photovoltaic performance, as noted in the previous sections, cell DU-35 was given special attention in the measurements. Firstly, to establish sufficient measurement accuracy, the cell was submitted to NREL for testing and Figure 5.8 is a comparison of current density-voltage curves measured under AMG 1.5 conditions. It is noted that there is good agreement between the NREL curve, measured on April 1st, and that measured at Montreal under the sun on March 13th 2003. Furthermore, Figure 5.9 shows a comparison of quantum efficiency versus wavelength plots measured in our laboratory and at NREL on April 2nd 2003. Again satisfactory agreement is evident, except at low wavelengths near 400nm. The data recorded on the cell at NREL on April 2nd for V_{oc} , j_{sc} , F.F, and η were respectively 0.497 volt, 35.3 mA/cm², 54.9 % and 9.6 % for a total cell area of 0.138 cm². If the effective area of the cell is used (total area minus area of two contact stripes) of 0.126 cm², then j_{sc} and η become 39 mA/cm² and 10.5 % respectively for the device without an antireflection coating.

Cell 35, in fact, had even better performance some months earlier, after it was first fabricated on December 23rd 2002. The first measurement under the sun was made on

January 7th 2003, when it yielded an apparent active-area conversion efficiency of some 12.5 %, assuming AMG 1.5 conditions. However, at that time, the pyranometer indicated an apparent solar irradiance of 90.5 mW/cm², that is below a full 100 mW/cm², for which the efficiency would have been higher at 13.7%. Current-voltage characteristics were measured at various dates after this under the sun and these plots are shown in Figure 5.10. Here, it is apparent that the photovoltaic performance degraded with time, particularly in respect of fill factor. The degradation is more clearly evident in Figure 5.11, where efficiency is plotted against storage time since fabrication.

5.5 DISCUSSION OF RESULTS

In the fabrication steps described in chapter 4, many factors can affect the performance of the cells. For example, it is believed that the rf sputtering conditions for depositing the ZnO are very important. However, beyond this, inspection of Table 5.1 suggests that higher conductance in the CuInSe₂ substrate is important as well. Thus, the better cells , DU-22-1 and 35, both have lower apparent dark series area resistances (column 8) and higher apparent hole concentrations (column 5 in Table 5.1, calculated from Mott Schottky plots in chapter 6). It is also of interest that cell 22-1 was cut from ingot 6, which had an excess of Se, although cell 35 was cut from ingot 3, prepared from a stoichiometric melt. It seems also, from the comparison of results with NREL, that our measurements were reasonably trustworthy.

From the results on cell 35, degradation over time was apparent. The device was given no special encapsulation against atmospheric exposure and the cause of the degradation is not known. In any case, the performance of this cell is superior to that of any

previously made cell using Bridgman-grown CuInSe_2 . This is not only in respect of original conversion efficiency but also of cell area, which is some 50 % larger than that of Yip and Shih [1.8]. It may be speculated from the low quantum efficiency that, with an effective anti-reflection coating, the original efficiency, when first fabricated, *could have even been higher than 15 %*. This is also taking into account the lower solar irradiance on January 7th 2003, when 12.5 % was recorded, but under AMG 1.5 conditions would have been 13.7%.

Table 5.1
Data measured on Au-CuInSe₂-CdS-ZnO-In Cells

Cell No.	CuInSe ₂ Ingot No.	CuInSe ₂ substrate thickness (mm)	Effect. cell area (mm ²)	Mott-Schottky ¹ acceptor concentration (10 ¹⁶ cm ⁻³)	Dark J-V ideality factor	J-V (slope) ¹ at 0.5V (Ωcm ²)		Conversion efficiency ^{2,3,4} , η (%)			Open circuit voltage ^{1,4} , V _∞ (V)		Short circuit current density ^{2,3,4} , j _{sc} (mA/cm ²)		Fill factor ^{3,4} , F.F. (%)	
						Solar simulator May 20th	Dark	Solar simulator May 20th	Sun May10th	Sun other	Solar simulator May 20th	Sun May10th	Solar simulator May 20th	Sun May10th	Solar simulator May 20th	Sun May10th
22-1	06	0.8	10.6	10.5	2.2	5.7	10	8.9	8.2	9.7 ⁵	0.48	0.47	39	43	47.5	40.5
24	04	1.8	20	2.4	2.7	6.3	15	6.5	6.3		0.45	0.45	32	33	45	42
33	03	1.2	12.4	5.7	2.2	9.4	19	6.1	6.1		0.45	0.45	39	35	35	39
35	03	1.0	12.6	10	2.1	2.3	4	10.7	9.4	13.7 ⁶	0.48	0.48	41	41	54	48
36	03	1.0	12.4	8.5	2.6	8.3	17	6.5	6.1		0.45	0.44	35	35	41	40

Notes:

- ¹ From Mott-Schottky slope at -1.5V.
- ² Effective cell area used.
- ³ Without A.R. coating.
- ⁴ Approximate irradiance 100mW/cm².
- ⁵ 9.3% measured under sunlight on Nov. 27th 2002, irradiance 96mW/cm².
- ⁶ 12.5% measured under sunlight on Jan. 7th 2003, irradiance 90.5mW/cm².

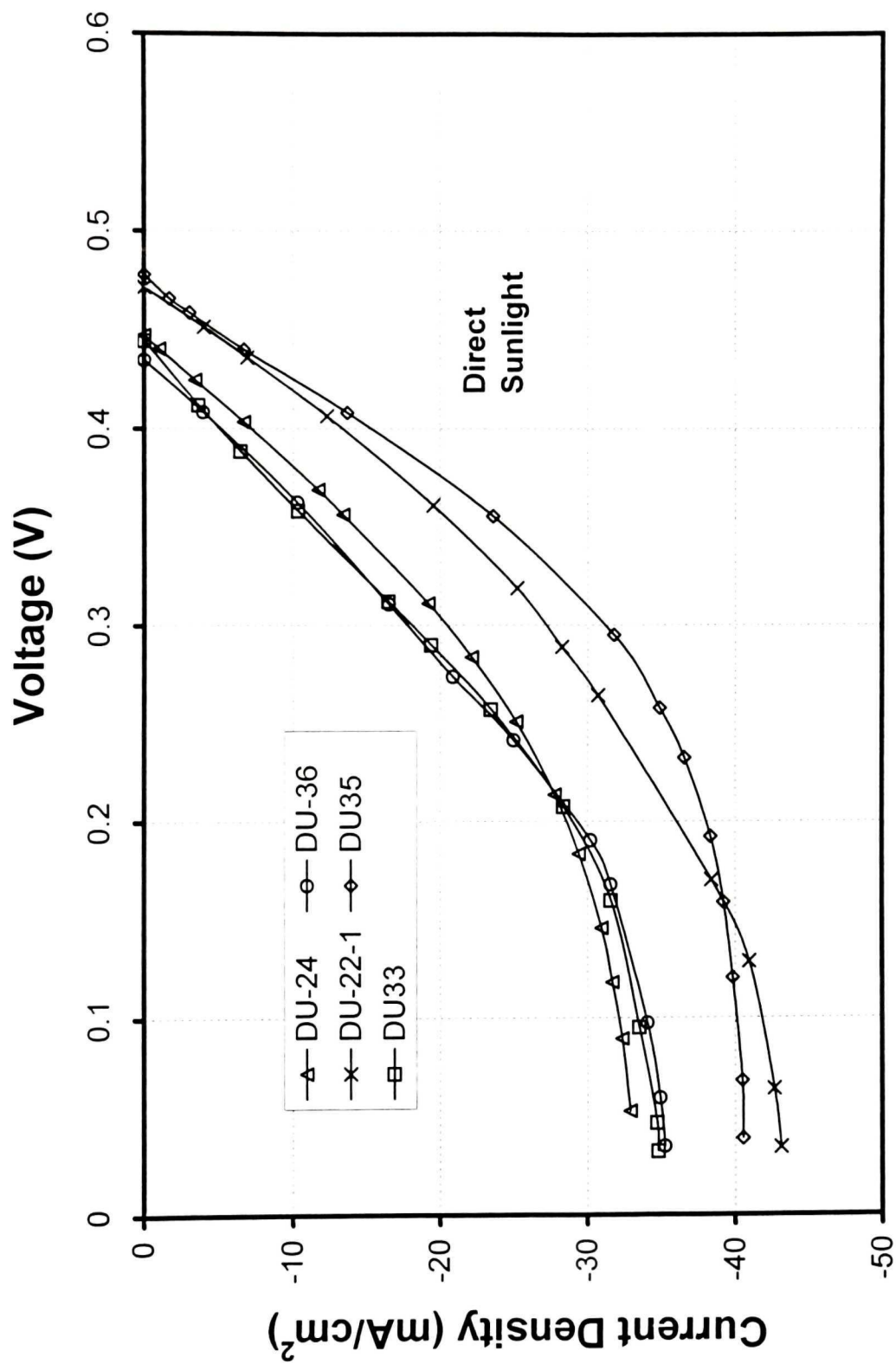


Figure 5.1 Current density-voltage characteristics of 5 cells measured under direct sunlight at noon in Montreal on May 10th, 2003.

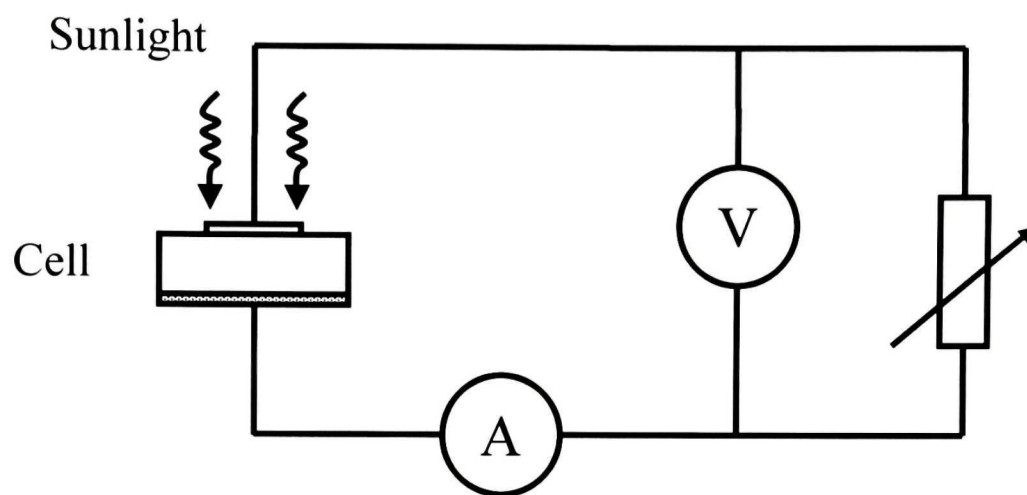


Figure 5.2 Arrangement for measuring the variation of current with voltage in a cell under actual sunlight.

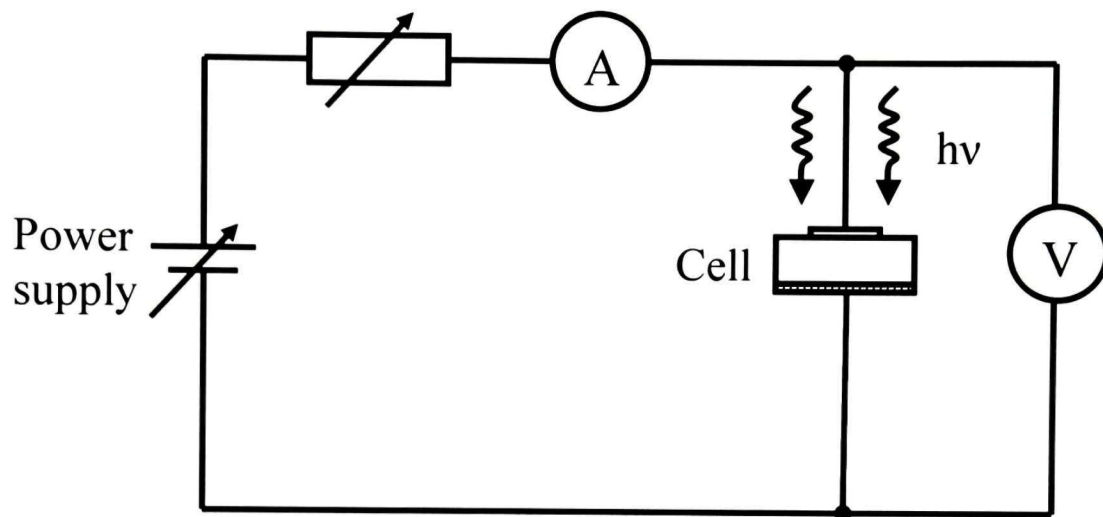


Figure 5.3 Arrangement to measure variation of current with voltage on a cell, under simulated solar irradiation, using a variable voltage source.

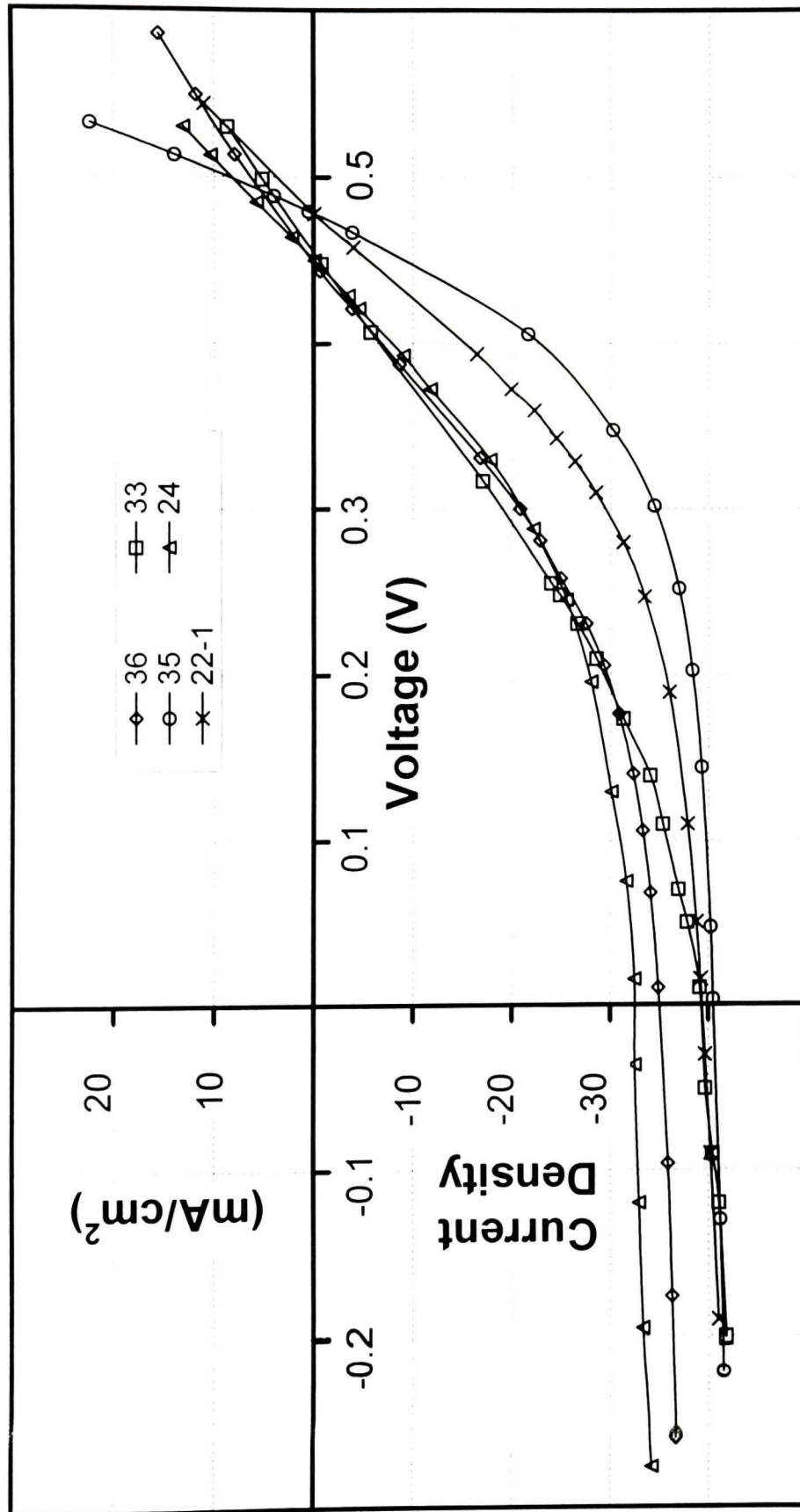


Figure 5.4 Current density-voltage characteristics of 5 cells measured under a solar simulator set at an irradiance of 100mW/cm²

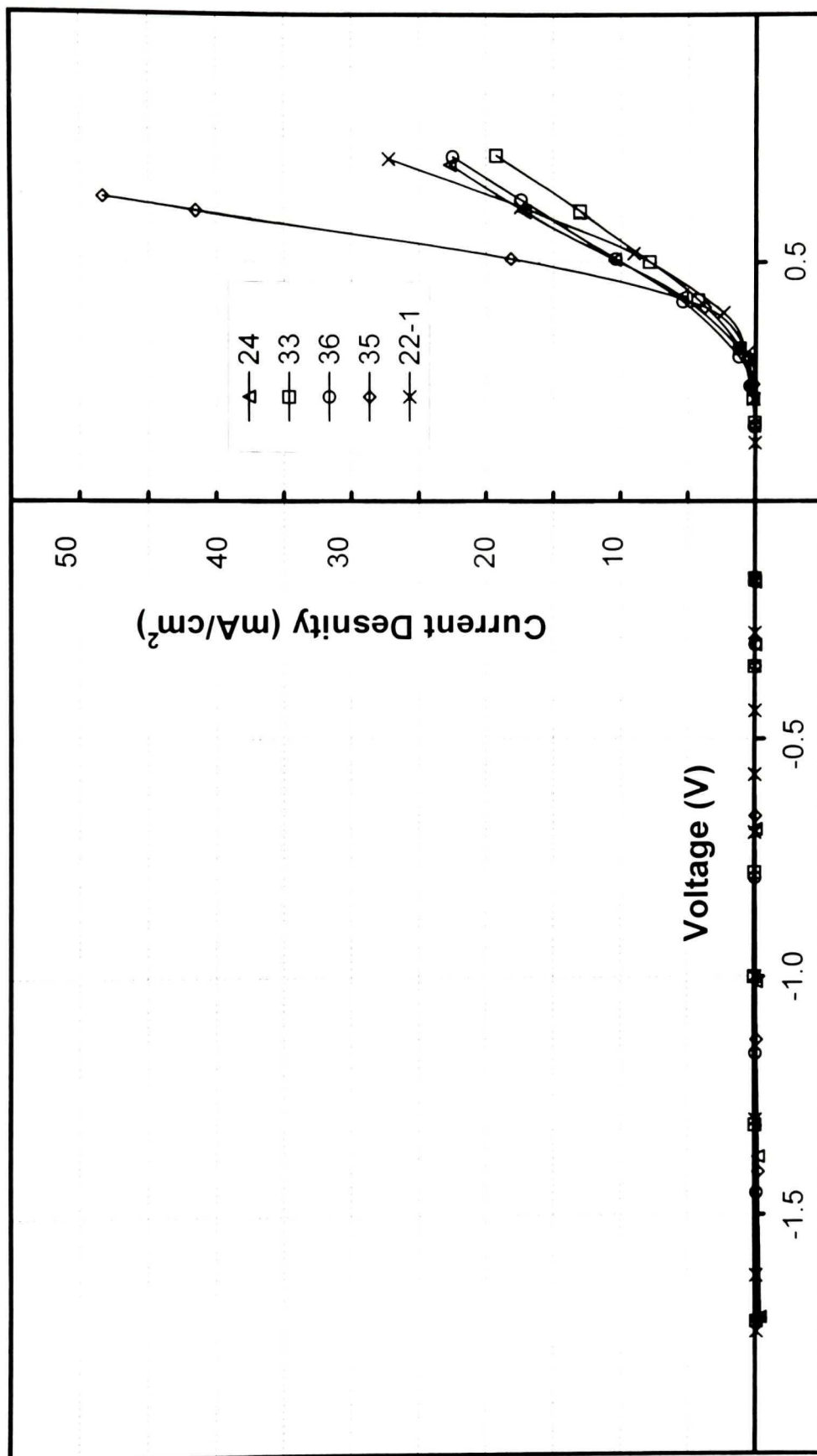


Figure 5.5 Current density-voltage characteristics of 5 cells measured under darkness.

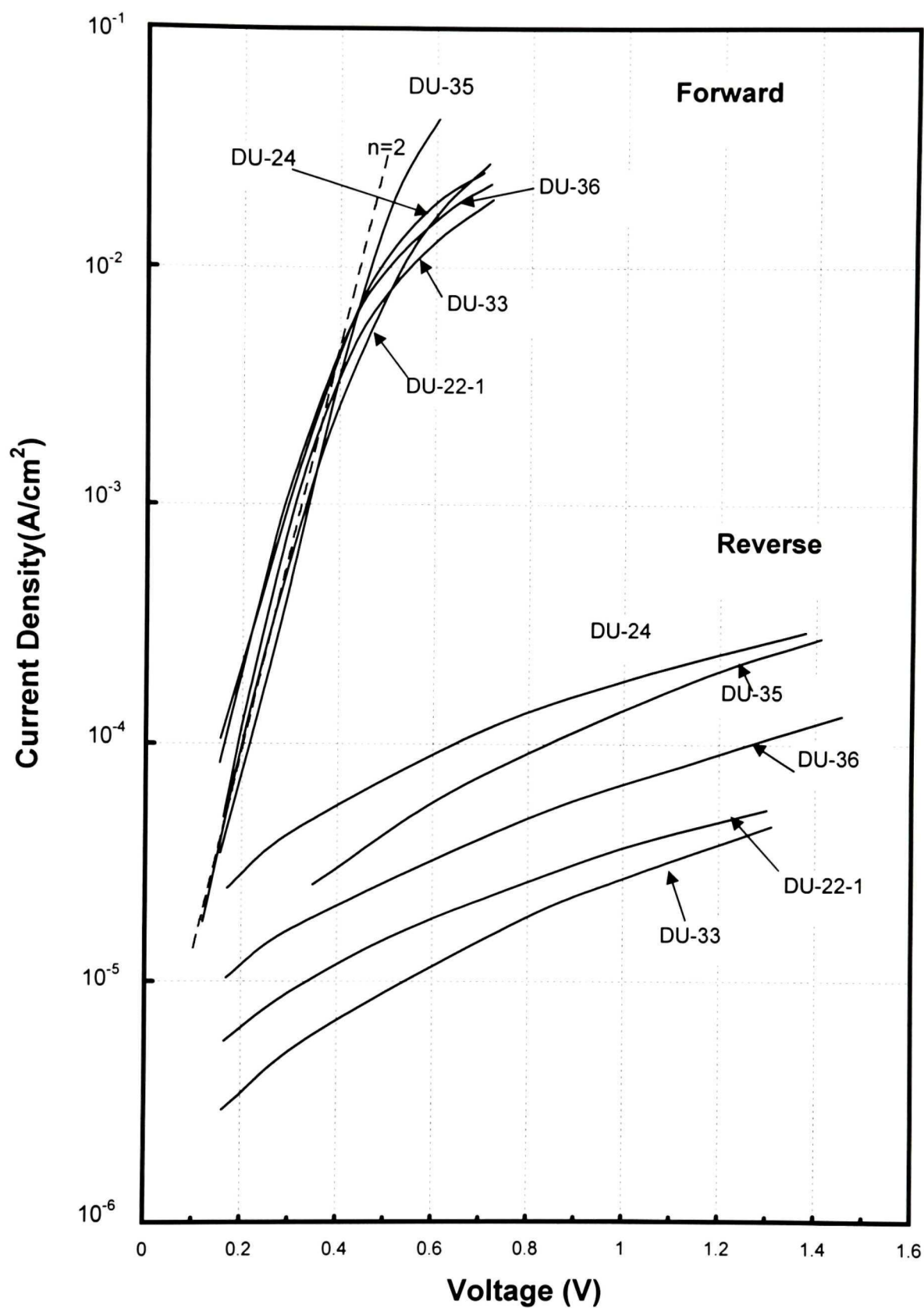


Figure 5.6 Plot of current density versus voltage, on semilogarithmic scales, for 5 cells measured under dark conditions.

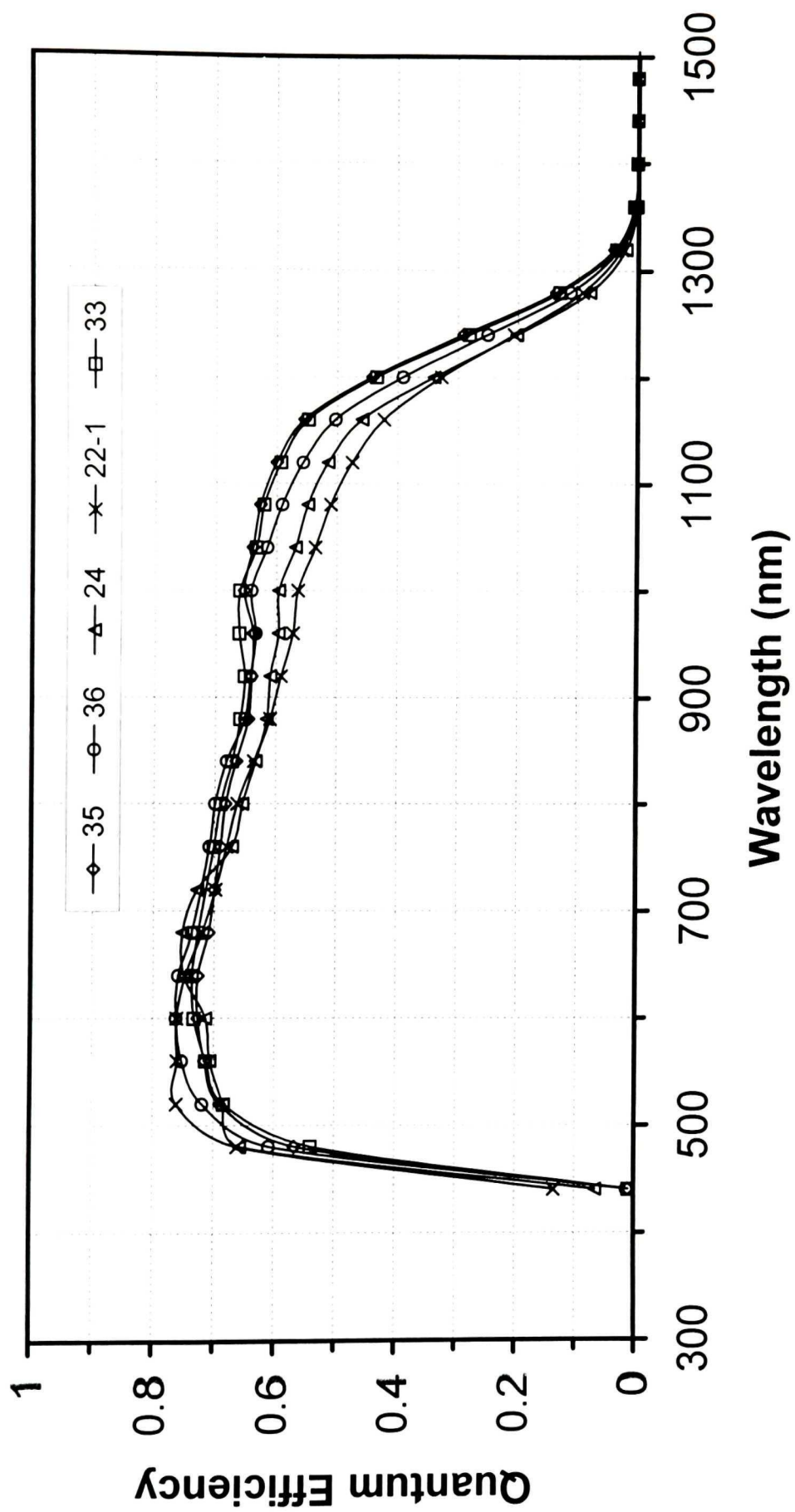


Figure 5.7 Quantum efficiency against wavelength for 5 cells at zero bias.

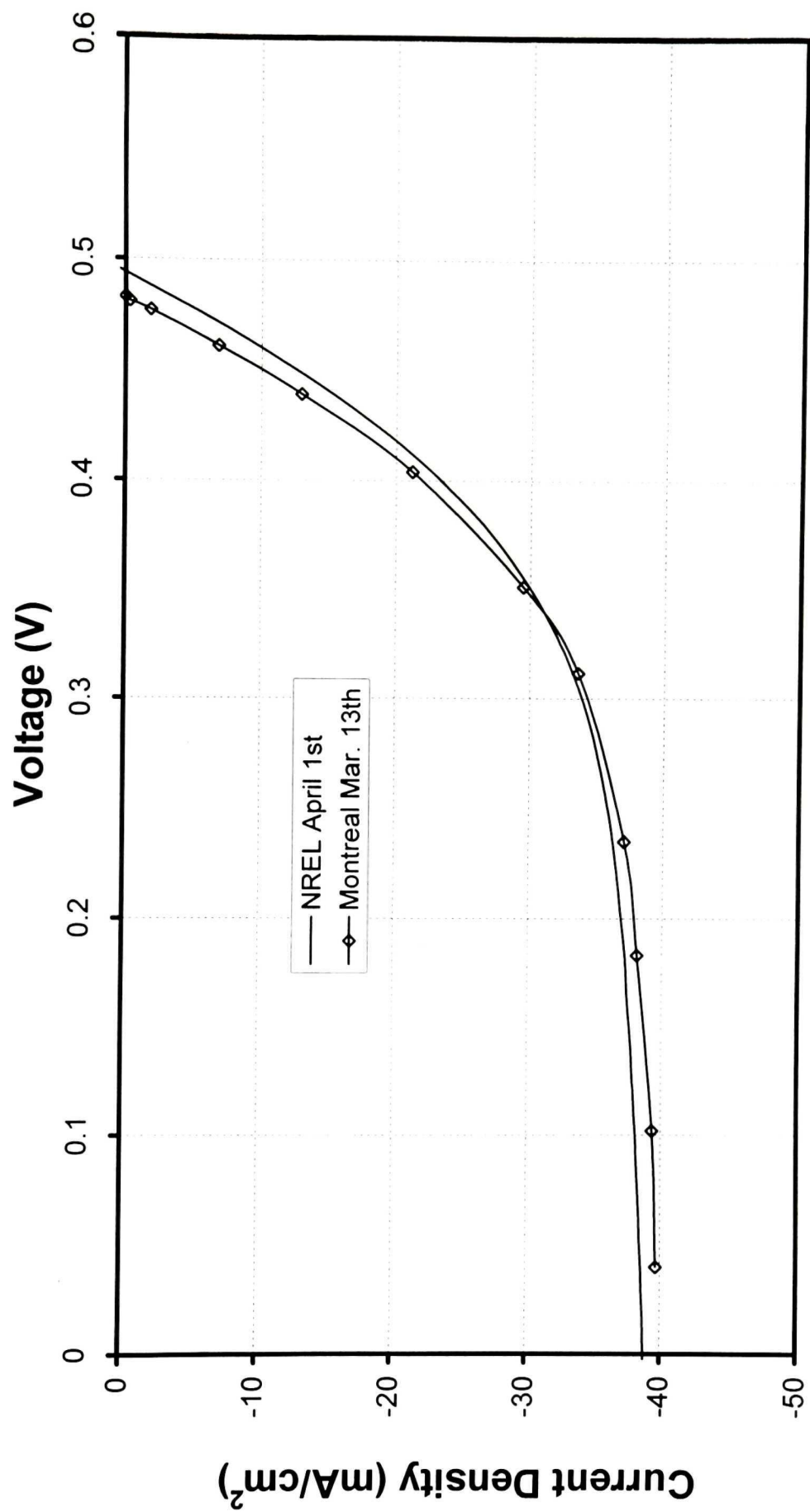


Figure 5.8 Comparison of current density-voltage characteristics of cell DU-35 from AMG 1.5 measurements at NREL on April 1st and from measurements under the sun in Montreal on March 13th, 2003.

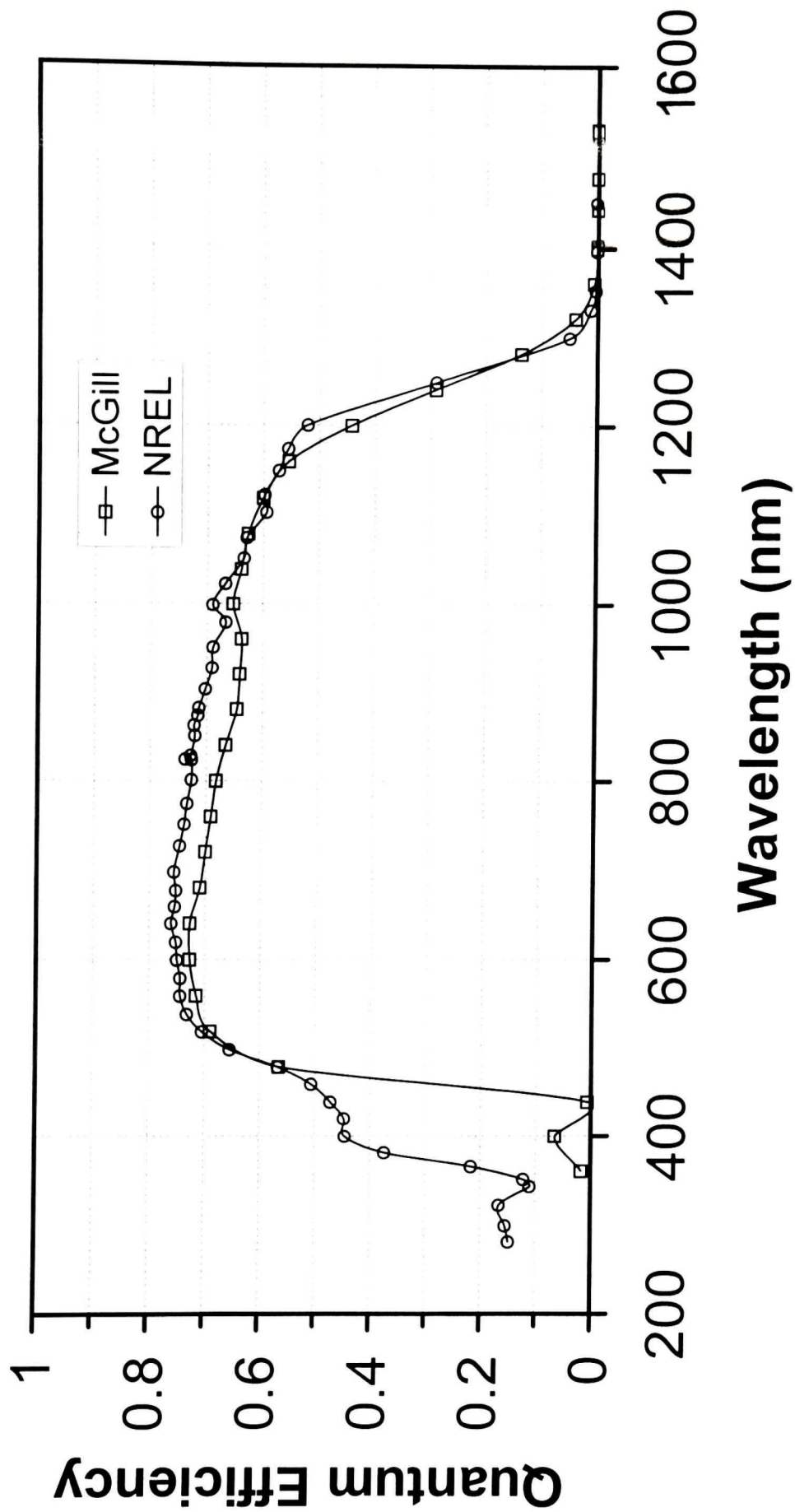


Figure 5.9 Comparison of quantum efficiency measurements on cell DU-35 made at NREL and at McGill University, Montreal.

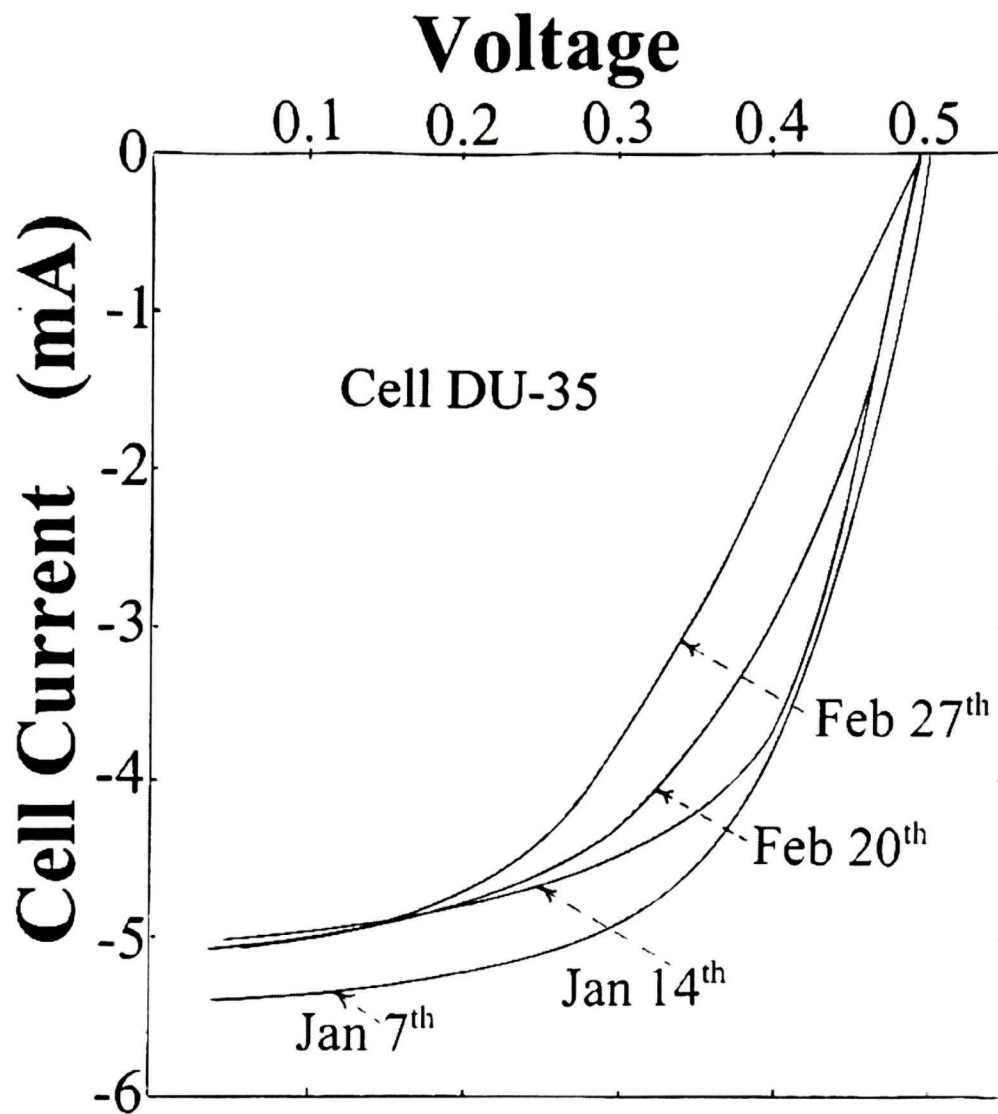


Figure 5.10 Current-voltage characteristics measured on cell DU-35 under sunlight in Montreal on 4 different dates in 2003. The cell was fabricated on December 23rd, 2002.

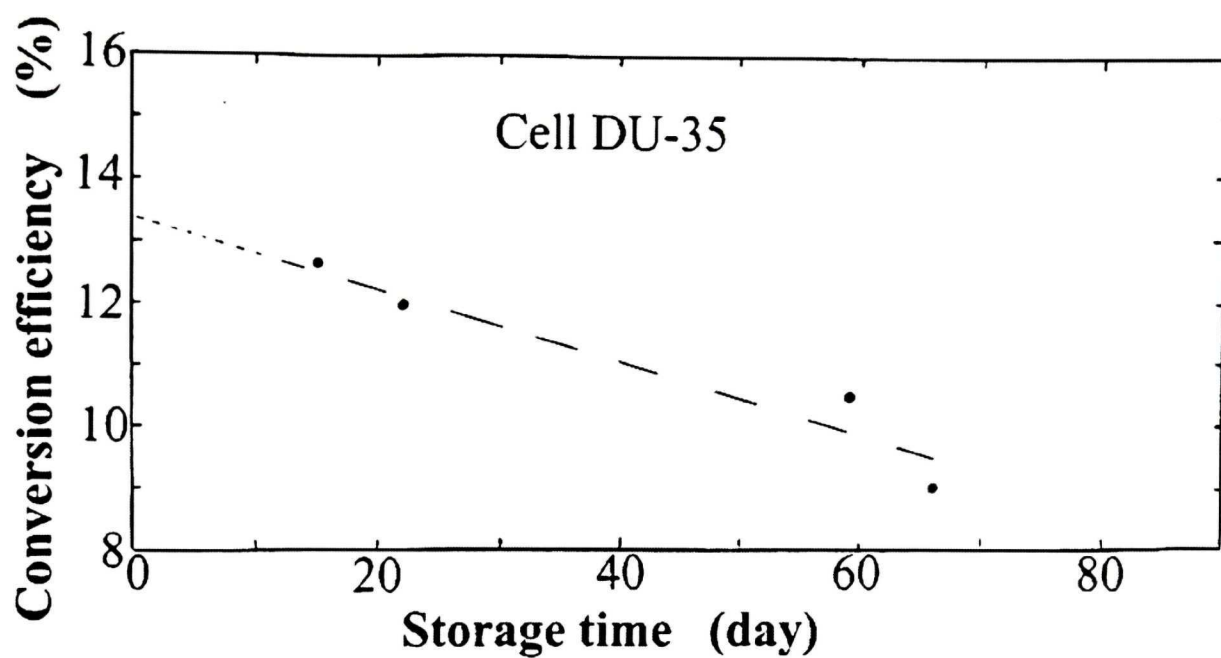


Figure 5.11 Plot of conversion efficiencies on cell DU-35, taken from Figure 5.10, against storage time since fabrication.

Chapter 6

Capacitance Measurements

6.1 INTRODUCTION

While the question is still unsettled as to whether the CuInSe_2 cells are heterojunctions or involve “buried” homojunctions, each of the devices fabricated here is assumed, at least, to have an n^+p junction, with a depletion layer, whose width is bias dependent. Thus, it is assumed that the depletion approximation applies for the reverse direction and that the depletion width extends mainly into the chalcopyrite, so that capacitance measurements can provide useful information about the p-type absorber layer of the cell. Accordingly, measurements of capacitance, C_p , in the parallel mode, were carried out on all the cells and the results are reported in this chapter. The variation of capacitance, at zero bias with frequency is first presented for all the cells and then the variation with bias (V) and frequency for cell 35 is shown. Following this, Mott-Schottky plots for cell 35 are given for different frequencies and finally Mott-Schottky plots for all the cells at a frequency of 10 kHz are presented.

6.2 MEASUREMENT SETTINGS

All the capacitance measurements were made, at room temperature, using a Hewlett Packard model 4192A Impedance Analyzer, with the signal level maintained at 20 mV, in the equivalent parallel circuit mode. Bias voltages applied to the cells were usually between

about +0.5 V (forward) and -1.5 V (reverse) and the frequencies employed were from 100 Hz to 1 MHz.

6.3 VARIATION WITH FREQUENCY

Figure 6.1 shows a plot of parallel capacitance per unit area (C_p/A) for zero bias as a function of frequency for all the cells. The variations show, except for cell 35, a general monotonic decrease of capacitance with frequency, with no indication of a plateau over the range covered.

6.4 Cell 35 - VARIATION WITH BIAS AND FREQUENCY

The variation of capacitance with frequency for cell 35 is shown in Figure 6.2 for 7 different values of applied bias, covering both forward (+) and reverse (-) directions. It is noted that, except for the two curves with forward bias, all the capacitance values show a minimum created by the final C_p rise at 1 MHz. Further, the curve for a bias of +0.4 V shows an anomalous rise at low frequencies, while the curve for the lower forward bias of +0.3 V shows an initial decrease, like the other curves for reverse bias. It is also noted that the range of capacitance variation with reverse bias was smaller at 1 MHz than at lower frequencies.

Figure 6.3 shows a Mott-Schottky plot for cell 35, measured at 5 different frequencies. At low frequencies, such as 100 Hz, fluctuating capacitance values were observed and this is evident in the scatter of the plotted experimental points for this frequency. Additionally, at 1 MHz, it is noted that the slope of the $(A/C_p)^2$ variation, with reverse bias, is less than that for the lower frequencies. Thus, to avoid the uncertainties at

low and high frequencies, a middle frequency of 10 kHz was chosen for the Mott-Schottky plots of all the cells.

6.5 MOTT-SCHOTTKY PLOTS

Mott-Schottky plots were obtained for all 5 cells at a frequency of 10 kHz and these are shown in Figure 6.4.

Using the formula for a one-sided junction [6.1]:

$$\frac{d\left[\left(\frac{A}{C_p}\right)^2\right]}{dV} = \frac{2}{\epsilon_0 \epsilon_r q N_A} ,$$

acceptor concentrations (N_A) were obtained from the slopes at a reverse voltage of - 1.5 V. Here, A is the cell area, ϵ_0 is the permittivity of vacuum and ϵ_r is the relative dielectric constant, taken as 10 for CuInSe₂. The values of N_A , so obtained, are listed in Table 5.1, column 5.

6.6 DISCUSSION

The capacitance measurements in this chapter were carried out principally to determine the relative differences in the acceptor or hole concentrations within the CuInSe₂ material, acting as the absorber layer in the cells. This appears to have been achieved, since the devices with the observed lower illuminated and dark series area resistances (Table 5.1, columns 7 and 8), cells 22-1 and 35, also had the higher values of N_A of some 10^{17} cm^{-3} from the Mott-Schottky plots.

There is also thus confidence that the selection of 10 kHz for the frequency in the capacitance measurements, for the Mott-Schottky plots, was a good choice. At low

frequency, much noise was experienced and at 1 MHz the variation of capacitance with bias was distinctly less than at lower frequencies.

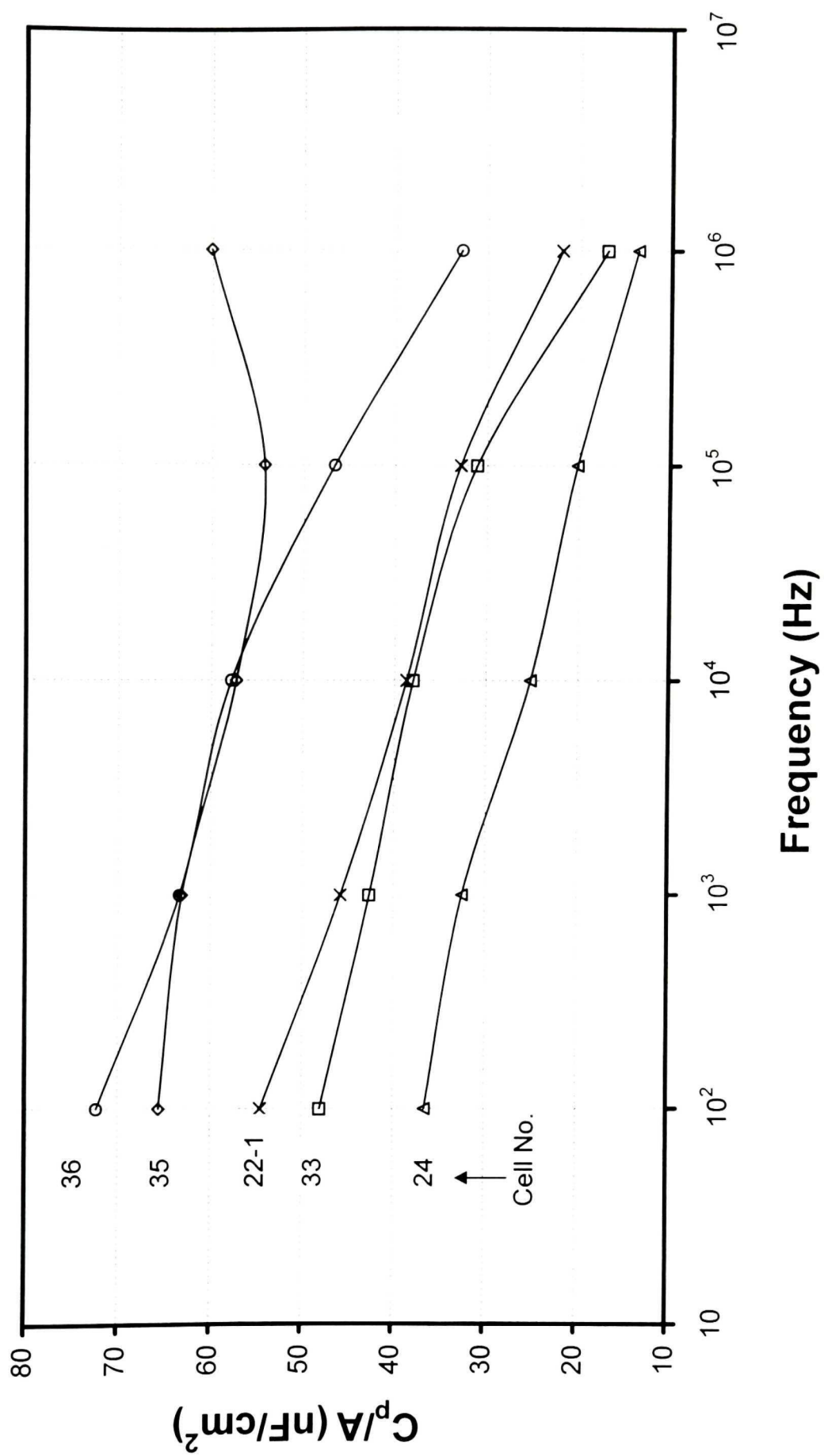


Figure 6.1 Variation of parallel capacitance per unit area with frequency for 5 cells at zero bias.

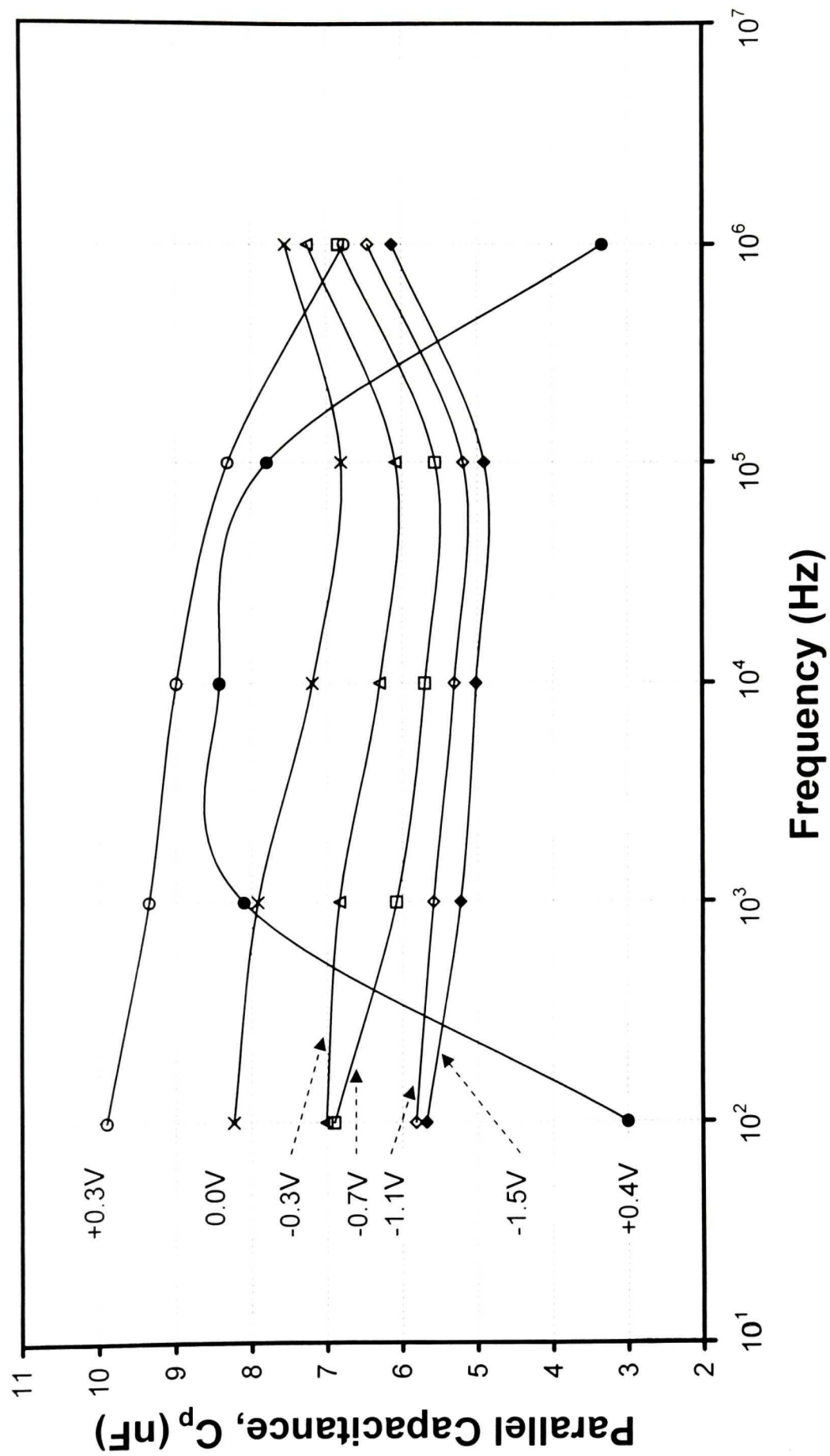


Figure 6.2 Parallel capacitance versus frequency for cell DU-35 at different bias voltages.

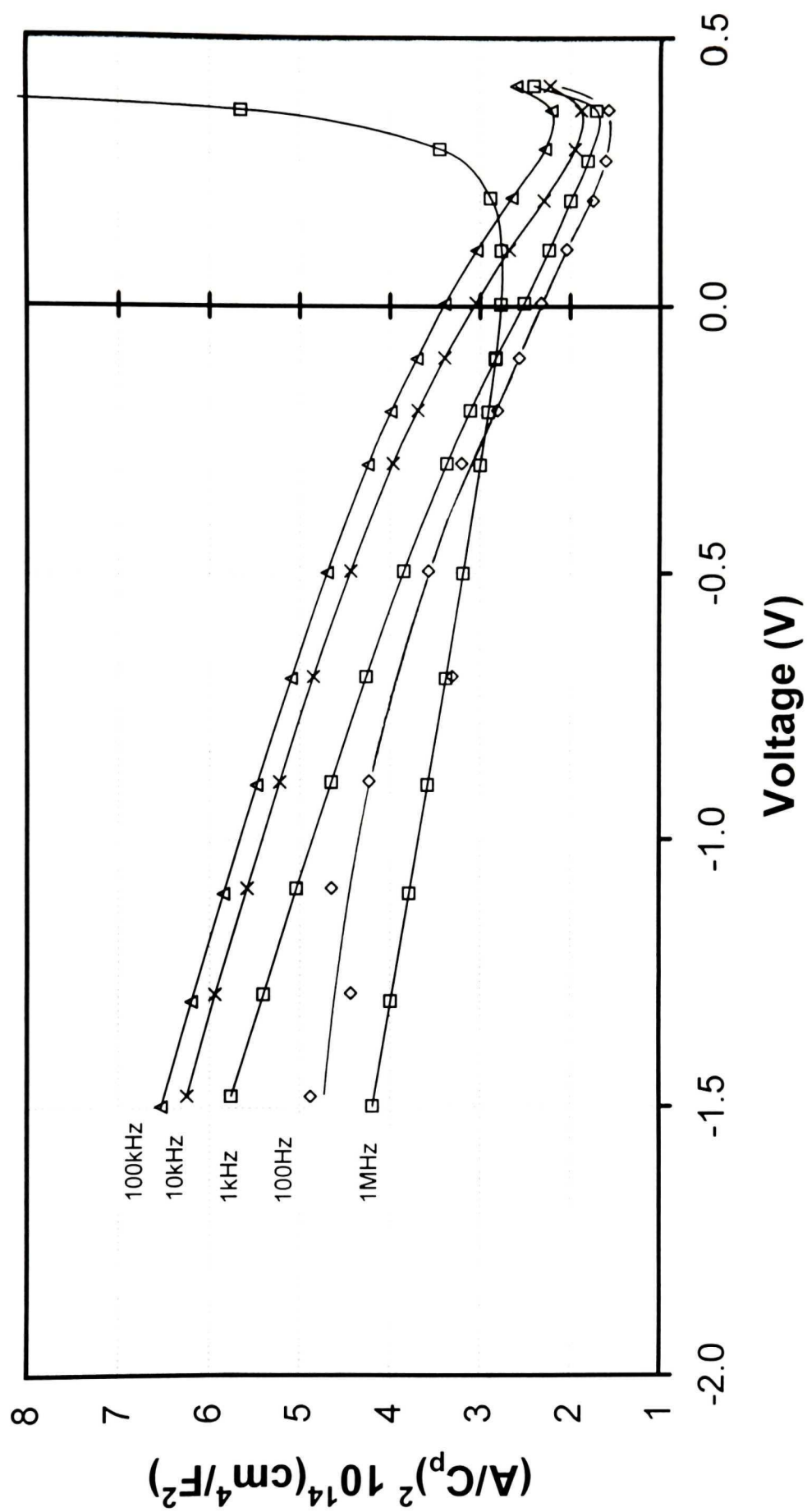


Figure 6.3 Mott-Schottky plot for cell DU-35 for 5 different frequencies.

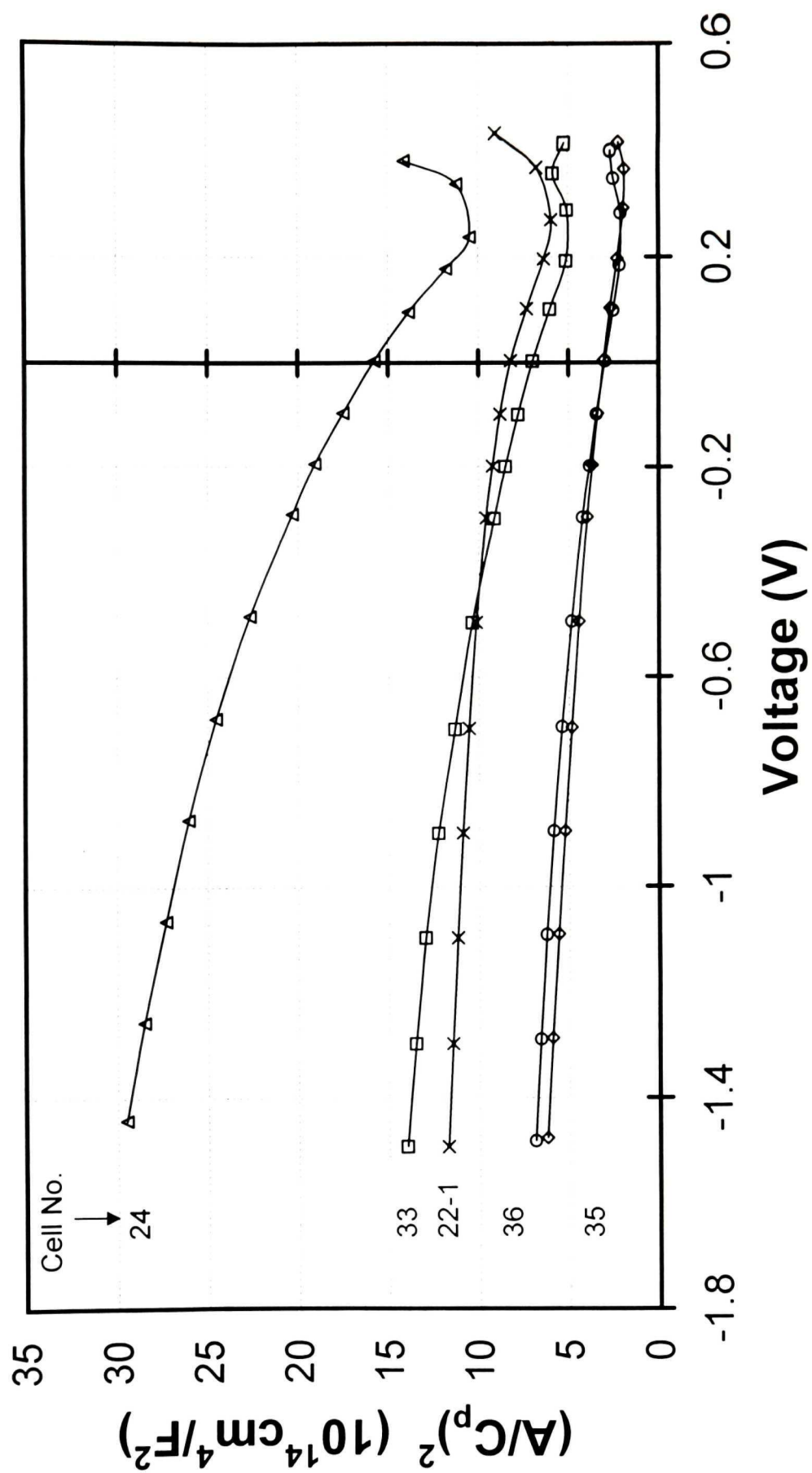


Figure 6.4 Mott-Schottky plots for 5 cells, measured at a frequency of 10 kHz.

Chapter 7

General Discussion and Conclusions

The chalcopyrite semiconductor CuInSe_2 is a unique material, with its chemical stability and high optical absorption in the visible region. While considerable work has been done on polycrystalline thin film structures of the compound, relatively few studies have been made on bulk monocrystalline material. This may be partly because of the perception that the preparation of single crystal material with uniform properties is difficult. However, work in the present laboratory has shown that this is not so, if certain procedures, in the Bridgman method, are used. Principally, these are:

- (1) Keep the starting elements in a strong-walled quartz ampoule for *both* compound synthesis and crystal growth [1.11]. If synthesis and Bridgman growth are carried out in separate vessels, this leads to loss of selenium and consequent ingot inhomogeneity.
- (2) Unless pure oxygen-free copper [7.1] is used, the ampoule should contain an oxygen getter; here, we have found that a flamed-in BN coating is very effective.
- (3) Post-growth annealing [1.4] in argon should be carried out for improved photovoltaic performance.

If these procedures are adopted, the Bridgman growth process is “forgiving” of small deviations from stoichiometry, yielding ingots which are uniformly single phase chalcopyrite and of uniform conductivity type in the main part of the ingot. Furthermore, there is no sticking of the ingot to the ampoule wall and little or no voids. Even in material

intentionally made from nonstoichiometric melts, these conditions apply in the main part of the resulting ingot, with other phases occurring in the last zone to freeze. Crystal size, within the ingot, was adequate in the present work but, since size appears to depend principally on the Bridgman furnace dimensions and on temperature profiles, there is room for improvement in the equipment used in our laboratory.

While the growth work in the present thesis followed that of previous workers in this laboratory, the following facts were confirmed. The solubility of excess copper in CuInSe_2 was confirmed to be small, in accordance with published phase diagrams [3.8]. Thus, precipitation of a copper phase occurred, even for the ingot with the melt composition $\text{Cu}_{1.1}\text{InSe}_2$. This took place mostly from the end of the ingot in the form of 30 micron diameter filaments, whose lattice parameters corresponded to those of copper with a 2 % increase, due to dissolved indium or selenium. There were no copper phase regions in the main part of the ingot but they did occur within the last zone to freeze. Here, an interesting and surprising observation was made that the four point probe resistivity immediately adjacent to a precipitated copper region was *higher* than elsewhere in the ingot, implying greater stoichiometry in these regions. Thus, it would appear that excess copper acts more as a compensator rather than having a doping role.

For deviations from stoichiometry involving selenium, excess of this element appeared to have no effect in the main part of the ingot but, in the last zone to freeze, the resistivity was reduced, implying a higher hole concentration there. By contrast, a deficiency of selenium had stronger effects, changing the ingot conductivity to n-type, with the main part single phase chalcopyrite but causing the end of the ingot to contain binary phases. One of these was identified as InSe . Other phases were reported by Shukri [3.6],

such as Cu_7In_4 and Cu_9In_4 .

Turning now to the photovoltaic cells made from the Bridgman material, a successful fabrication procedure was developed and results on 5 of the cells are reported here. Of these, one device, cell 35, was found to give a photovoltaic performance superior to any monocrystalline cell previously prepared, both in conversion efficiency and cell area. With an effective area some 50% larger than that of Yip and Shih in 1994 [1.8], cell 35 yielded an active-area conversion efficiency of about 12.5 %, without an antireflection coating, under the sun with an irradiance of 90.5 mW/cm^2 , that is less than AMG 1.5 conditions. It also exhibited fill factor degradation with storage time and showed quantum efficiencies generally below 80 %, so that with an effective A.R. coating, the cell, nearer the time of fabrication could have had an AMG 1.5 efficiency of over 15 %. Thus, this may have even exceeded the record for any CuInSe_2 cell. While, such an efficiency claim is somewhat speculative, the trustworthiness of the measurements is not in doubt, since the illuminated current-voltage and quantum efficiency characteristics were checked at NREL on this cell.

The two best cells, 22-1 and 35, both had higher apparent hole concentrations of about 10^{17} cm^{-3} , obtained from slopes of their Mott-Schottky plots. These cells also had lower illuminated series area resistances. Cell 35 was prepared from a stoichiometric ingot , while cell 22-1 was obtained from an ingot with excess selenium. Cells prepared from ingots with excess copper (not reported), gave poor photovoltaic performance.

In the cell preparation, only one layer of doped ZnO was deposited, whereas in many thin film polycrystalline devices there are two ZnO layers [4.2], one doped and the other undoped of high resistivity. Some initial experiments with two ZnO layers were made

on Bridgman material substrates but these did not yield better cells.

Thus overall, it would seem, from the present work, that it is possible to fabricate cells from Bridgman-grown CuInSe_2 , which can equal and perhaps exceed the performance of the best thin film polycrystalline cells. While, there would be no economic incentive to do this for commercial devices, much extra knowledge could be gained by further work about factors such as optimal crystal orientation, the role of cadmium and sodium and that of ordered valency compounds like CuIn_3Se_5 . Beyond this, work is needed also on cells made with monocrystalline quaternary chalcopyrites, such as Cu(In,Ga)Se_2 .

References

- [1.1] K. Ramanathan, M.A. Contreras, C.L. Perkins, S. Asher, F.S. Hasoon, J. Keane, D. Young, M. Romero, W. Metzger, R. Noufi, J. Ward and A. Duda. *Properties of 19.2% efficiency ZnO/CdS/CuInGaSe₂ thin-film solar cells*. Progress in Photovoltaics: Research and Applications **11** (2003) 225-230.
- [1.2] H. Schock, K. Bogus. *Development of CIS solar cells for space applications*. 2nd World Conference and Exhibition on Photovoltaic Solar Energy Conversion (1998) 3586-3589.
- [1.3] T. Dullweber, O. Lundberg, J. Malmström, M. Bodegård, L. Stolt, R. Rau, H.W. Schock and J. Werner. *Back surface band gap gradings in Cu(In,Ga)Se₂ solar cells*. Thin Solid Films **387** (2001) 11.
- [1.4] L.S. Yip. *Development of high-efficiency solar cells on CuInSe₂ single crystals*. Ph.D. Thesis, McGill University (1996).
- [1.5] J.L. Shay, S. Wagner and H.M. Kasper. *Efficient CuInSe₂/CdS solar cells*. Applied Physics Letters **27** (1975) 89-90.
- [1.6] L.L. Kazmerski and P. Sheldon. *Fabrication and characterization of ITO/CuInSe₂ photovoltaic heterojunctions*. Proceedings 13th IEEE Photovoltaic Specialists Conference (1978) 541.
- [1.7] R.R. Aray, T. Warminski, R. Beaulieu, M. Kwietniak, J.J. Loferski and W. Giriat. *Photovoltaic and structural properties of CuInSe₂/CdS solar cells*. Solar Energy Materials **8** (1983) 471-481.
- [1.8] L.S. Yip and I. Shih. *Photovoltaic cells with efficiency exceeding 10% using monocrystalline CuInSe₂ substrates*. IEEE Photovoltaic Specialists Conference **1** (1994) 210-213.
- [1.9] M.A. Green, K. Emery, D.L. King, S. Igari and W. Warta. *Solar cell efficiency tables (version 21)*. Progress in Photovoltaics: Research and Applications **11** (2003) 39-45.
- [1.10] C.H. Champness. *Melt-grown CuInSe₂ and photovoltaic cells*. Journal of Materials Science: Materials in Electronics **10** (1999) 605-622.
- [1.11] Z.A. Shukri. *Bridgman growth of CuInSe₂ monocrystals for photovoltaic cell research*. Ph.D. Thesis, McGill University (1996).

- [1.12] G.I. Ahmad. *Electrical investigations on CuInSe₂ single crystals*. M.Eng. Thesis, McGill University (1996).
- [2.1] H.J. Hovel. *Semiconductor and semimetals, volume II, solar cells*. Academic Press, New York (1975)
- [2.2] M.A. Green. *Solar cells*. Prentice-Hall, N.J. (1982).
- [2.3] M.D. Archer and R. Hill. *Clean electricity from photovoltaics*. Imperial College Press, London (2001).
- [2.4] K. Mitchell and H.Schock. *Thin film photovoltaic technologies*. Tutorial Notebook, 23rd IEEE Photovoltaic Specialists Conference (1993).
- [2.5] J.R. Tuttle, R. Noufi and R.G. Dhere. *The effect of composition on the optical properties of CuInSe₂ thin films*. 19th IEEE Photovoltaic Specialists Conference (1987) 1494-1495.
- [3.1] Z.A. Shukri, C.H. Champness and I. Shih. *Boron nitride powder coating of ampoule for Bridgman-grown CuInSe₂*. Journal of Crystal Growth **129** (1993) 107-110.
- [3.2] Z.A. Shukri and C.H. Champness. *Cleavage and twinning in CuInSe₂ crystals*. Acta Crystallographica **B53** (1997) 620.
- [3.3] J. Parkes, R.D. Tomlinson and M.K. Hampshire. *The fabrication of p and n type single crystals of CuInSe₂*. Journal of Crystal Growth **20** (1973) 315.
- [3.4] R.M. Warner. *Integrated circuits, Motorola series in solid-state electronics*. McGraw-Hill (1965) 80-81.
- [3.5] P.D. Ankrum. *Solid state physical electronics series, semiconductor electronics*. Prentice-Hall, N.J. (1971) 11-12.
- [3.6] Z.A. Shukri and C.H. Champness, *Effect of nonstoichiometry on conductivity type in Bridgman-grown CuInSe₂*. Journal of Crystal Growth **191** (1998) 97.
- [3.7] L.L. Kazmerski. *Array to atoms: the evolution of characterization*. 23rd IEEE Photovoltaic Specialists Conference (1993) 1.
- [3.8] L.S. Palatnik and E.I. Rogacheva. *Phase diagrams and structure of some semiconductor A₂^IC^{VI}-B₂^{III}C^{IV} alloys*. Soviet Physics-Doklady **12** (1967) 503-506.
- [4.1] A.A. Al-Quraini. *Monocrystalline CuInSe₂ photovoltaic cells with a CdO window layer*. M.Eng. Thesis, McGill University (1998).

- [4.2] J. Kessler, M. Ruckh, D. Hariskos, U. Ruhle, R. Menner and H.W. Schock. *Interface engineering between CuInSe₂ and ZnO* 23rd IEEE Photovoltaic Specialists Conference (1993) 447-452.
- [6.1] D.A. Neaman. *Semiconductor physics and devices, basic principles*. Second Edition, Irwin (1997) 227.
- [7.1] Z.A. Shukri and C.H. Champness. *Identification of oxygen in the copper as the source of adhesion in Bridgman-grown CuInSe₂ crystals*. Journal of Crystal Growth **166** (1996) 708-711.